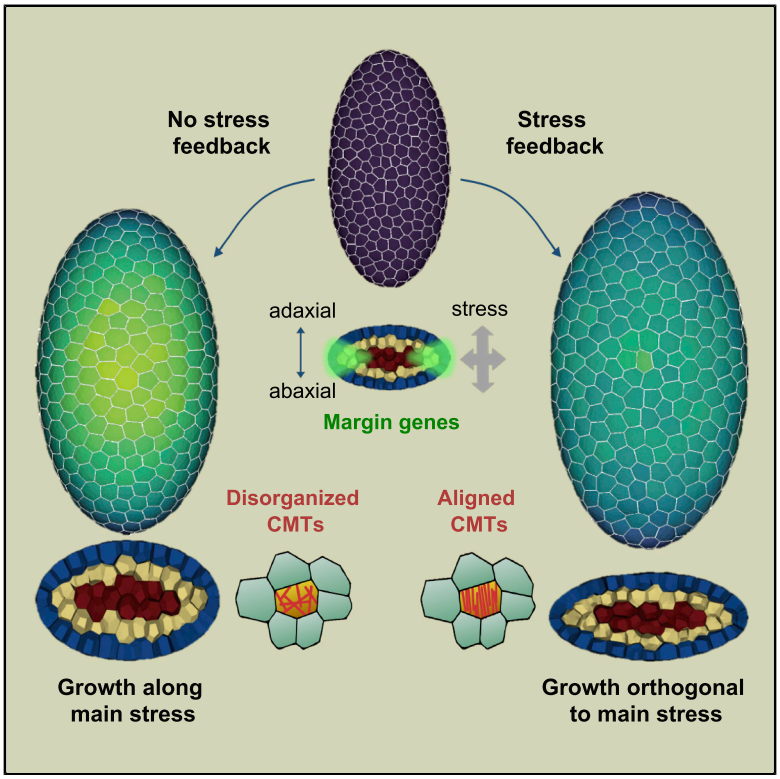
Article

Current Biology

Microtubule-Mediated Wall Anisotropy Contributes to Leaf Blade Flattening

Graphical Abstract



Authors

Feng Zhao, Fei Du, Hadrien Oliveri, ..., Christophe Godin, Jan Traas, Yuling Jiao

Correspondence

jan.traas@ens-lyon.fr (J.T.), yljiao@genetics.ac.cn (Y.J.)

In Brief

How do leaves maintain highly directional cell growth and divisions to form thin, flat laminae? Zhao et al. show that microtubules and cellulose microfibrils align along the main stress direction of internal walls to mediate anisotropic growth. Microtubule-mediated mechanical feedback amplifies an initial asymmetry and maintains directional growth.

Highlights

- Microtubules and cellulose microfibrils align along the ad-abaxial direction
- Microtubule-mediated cell growth anisotropy contributes to leaf flattening
- Mechanical feedback accounts for microtubule alignments in the ad-abaxial direction
- Final organ shape depends on the degree of initial asymmetry of primordia

Zhao et al., 2020, Current Biology *30*, 3972–3985
October 19, 2020 © 2020 The Author(s). Published by Elsevier Inc.
https://doi.org/10.1016/j.cub.2020.07.076

CellPress

CellPress
OPEN ACCESS

Current Biology

Article

Microtubule-Mediated Wall Anisotropy Contributes to Leaf Blade Flattening

Feng Zhao,[1,7] Fei Du,[2,7] Hadrien Oliveri,[1,7] Lüwen Zhou,[3,7] Olivier Ali,[1,7] Wenqian Chen,[1] Shiliang Feng,[3] Qingqing Wang,[2,4] Shouqin Lü,[4,5] Mian Long,[4,5] René Schneider,[6] Arun Sampathkumar,[6] Christophe Godin,[1] Jan Traas,[1,*] and Yuling Jiao[2,4,8,*]

[1]Laboratoire Reproduction et Développement des Plantes, Univ Lyon, ENS de Lyon, UCB Lyon 1, CNRS, INRAE, Inria, 69342 Lyon, France
[2]State Key Laboratory of Plant Genomics and National Center for Plant Gene Research (Beijing), Institute of Genetics and Developmental Biology, The Innovative Academy of Seed Design, Chinese Academy of Sciences, Beijing 100101, China
[3]Smart Materials and Advanced Structure Laboratory, School of Mechanical Engineering and Mechanics, Ningbo University, Ningbo, Zhejiang 315211, China
[4]University of Chinese Academy of Sciences, Beijing 100049, China
[5]Key Laboratory of Microgravity (National Microgravity Laboratory), Center of Biomechanics and Bioengineering, and Beijing Key Laboratory of Engineered Construction and Mechanobiology, Institute of Mechanics, Chinese Academy of Sciences, Beijing 100190, China
[6]Max Planck Institute of Molecular Plant Physiology, Am Mühlenberg 1, 14476 Potsdam-Golm, Germany
[7]These authors contributed equally
[8]Lead Contact
*Correspondence: jan.traas@ens-lyon.fr (J.T.), yljiao@genetics.ac.cn (Y.J.)
https://doi.org/10.1016/j.cub.2020.07.076

SUMMARY

Plant organs can adopt a wide range of shapes, resulting from highly directional cell growth and divisions. We focus here on leaves and leaf-like organs in *Arabidopsis* and tomato, characterized by the formation of thin, flat laminae. Combining experimental approaches with 3D mechanical modeling, we provide evidence that leaf shape depends on cortical microtubule mediated cellulose deposition along the main predicted stress orientations, in particular, along the adaxial-abaxial axis in internal cell walls. This behavior can be explained by a mechanical feedback and has the potential to sustain and even amplify a preexisting degree of flatness, which in turn depends on genes involved in the control of organ polarity and leaf margin formation.

INTRODUCTION

The emergence of complex organ shapes with various degrees of asymmetry is an outstanding question in developmental biology. In plants, above-ground organs can broadly be classified into leaves (phyllomes) and stems (caulomes), each with a wide range of variations in shape [1]. We focus here on leaves and leaf-like organs. A common trait is the formation of a thin leaf lamina, considered as an important adaptation that optimizes vital processes, including photosynthesis, transpiration, and respiration [2].

The molecular regulatory networks involved in the development of leaves and leaf-like organs have been relatively well characterized [2, 3]. In particular, a highly conserved set of genes has been identified, which determines adaxial-abaxial (ad-abaxial) polarity and is essential for the establishment of leaf shape [4, 5]. In *Arabidopsis*, these encode transcription factors like ASYMMETRIC LEAVES1 and 2 (AS1, AS2), KANADI1, or FILAMENTOUS FLOWER, often active in either the adaxial or the abaxial domain to promote corresponding domain identity. Regulatory genes expressed in each domain also suppress genes expressed in the other. The adaxial and abaxial regulators further define the middle domain in between, which encompasses the leaf margin. In *Arabidopsis*, the middle domain is characterized by the expression of two *WUSCHEL RELATED HOMEOBOX* (*WOX*) genes, *WOX1* and *PRESSED FLOWER* (*PRS*). Perturbing the ad-abaxial and/or margin identity can severely affect leaf shape and the degree of flatness. In extreme cases, this can even lead to a complete loss of leaf asymmetry and the formation of axisymmetric leaves.

Combining theoretical and quantitative experimental approaches, recent studies have addressed the regulation of leaf geometry in a variety of species (e.g. [6–9]). These studies have mostly analyzed how different geometries of the leaf blade emerge from heterogeneous patterns of cell division and expansion. In this context, the functions of several genes have been expressed in terms of growth rates and directions, without considering the biophysical mechanisms that translate molecular regulation into geometrical output. To control the geometry, molecular regulation has to interfere with the mechanical properties of the tissues and/or the turgor pressure driving growth. Mechanically, growth in plants is related to the irreversible, anelastic deformation of the cell walls in response to turgor pressure [10–12]. Previous work has convincingly shown that the regulation of the anisotropic mechanical properties of the walls is key in shaping organs. In particular, membrane-associated cortical microtubules (CMTs) control the deposition of stiff cellulose microfibrils in specific orientations, thus limiting growth in those

 © 2020 The Author(s). Published by Elsevier Inc.
This is an open access article under the CC BY-NC-ND license (http://creativecommons.org/licenses/by-nc-nd/4.0/).

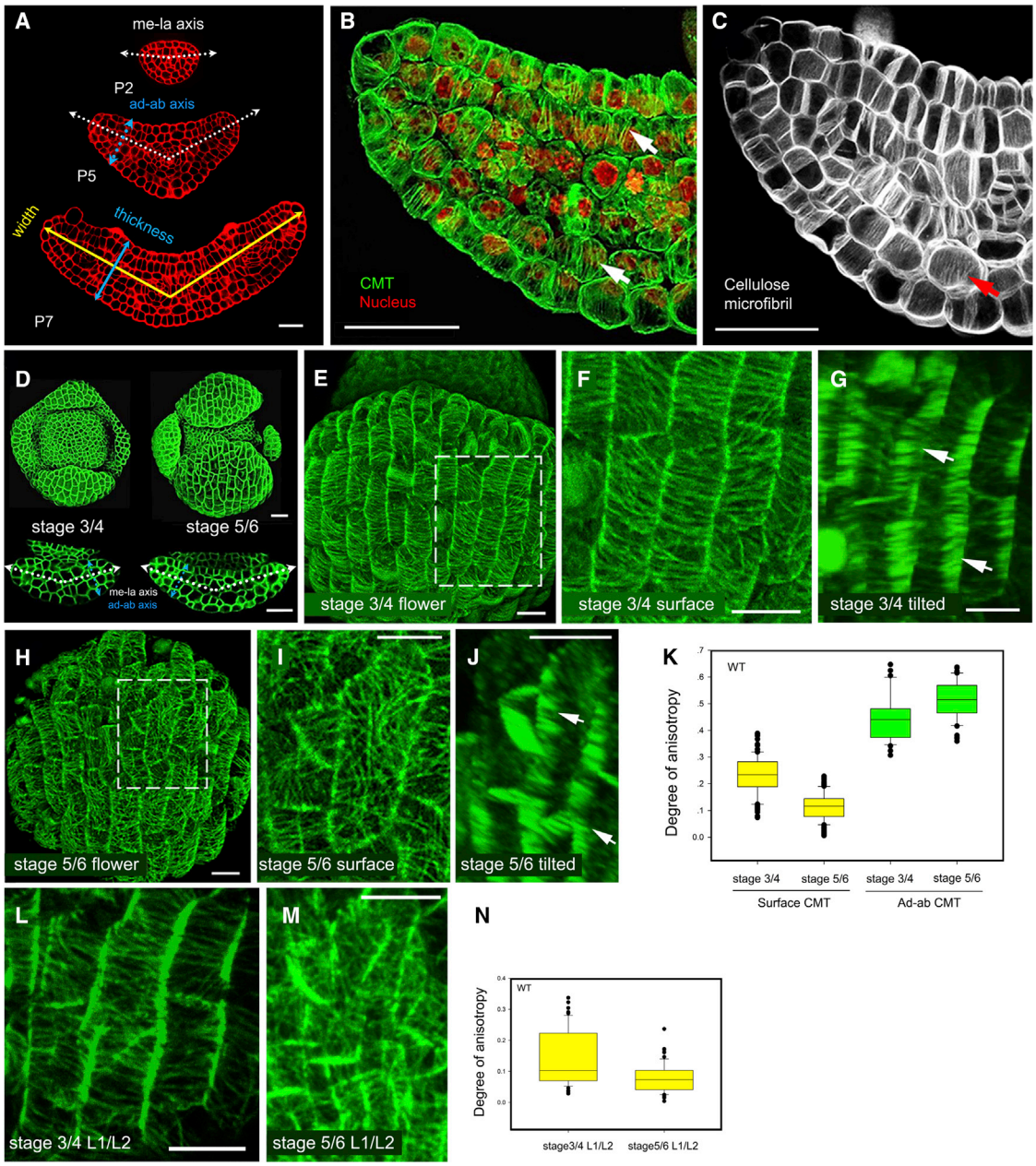


Figure 1. Shape, CMT Organization, and Cell Division in Developing Leaves and Sepals

(A) Cross sections of *Arabidopsis* leaf primordia showing highly anisotropic growth.

(B and C) CMT organization by immunostaining (green) with nuclei stained by DAPI (red) (B) and cellulose microfibrils stained by Direct Red 23 (white) in *Arabidopsis* rosette leaf primordia (C). White and red arrows indicate highly anisotropic CMTs and cellulose microfibrils, respectively, in the ad-abaxial direction.

(D) Overview of the same flower bud and cross sections through the abaxial sepal at flower stages 3/4 and 5/6.

(E–I) Sepals expressing GFP-MBD. (E) Overview of a sepal at stage 3/4, inset indicates detail given in (F) showing anisotropic CMTs at the outer surface walls. (G) Same image stack as (F) but tilted to show highly anisotropic ad-abaxial CMTs (arrows). (H) Overview of a sepal at stage 5/6, inset indicates detail given in (I) to show isotropic CMTs.

(J) titled image of (I) showing anisotropic CMTs in walls in the ad-abaxial direction (arrows).

(K) Quantification of CMTs on surface walls and walls in the ad-abaxial direction in sepals using *Fibriltool* [17], showing differences in the degree of anisotropy along ad-abaxial walls (n = 32 walls from 4 stage 3/4 sepals; n = 52 walls from 5 stage 5/6 sepals; $p < 0.001$ by Student's t test) and outer surface walls (n = 100 cells from 4 stage 3/4 sepals; n = 207 cells from 5 stage 5/6 sepals) walls during sepal development. Boxplots represent the interquartile range, split by the median, and whiskers indicate the total range; outliers are plotted as individual pots.

(L) same areas in (F) showing anisotropic CMTs at the interface of L1/L2 walls.

(legend continued on next page)

directions and driving growth anisotropy [13, 14]. The coordination of this mechanical regulation during the development of entire tissues and organs is an extremely complex issue, which remains poorly understood. It has started to be addressed using classical genetic and cellular approaches combined with computational models. When it comes to leaf development, studies addressing tissue mechanics in 2D have either considered development in the plane of the leaf blade or in cross sections including internal cells [11, 12]. So far, however, the geometrical and mechanical complexity of its cellular structure was not considered in all three dimensions.

Using experimental analysis and computational modeling, we have explored the mechanical basis of morphogenesis in leaves and leaf-like organs in 3D. To place our analysis in a broader context, two species (*Arabidopsis thaliana* and *Solanum lycopersicum*) were used, and different leaf-like organs were examined. We have identified an organ-wide biomechanical regulation of microtubule-based growth anisotropy. Simulations and experimental data suggest that this involves coordinated alignment of microtubules along predicted mechanical stress, primarily in internal tissues. The resulting anisotropic wall reinforcement would then maintain and amplify directional growth and organ flatness during early stages of development. We propose that mechanical feedback contributes to leaf flattening, in concert with genes involved in the definition of leaf polarity.

RESULTS

CMT Alignment during the Early Development of Leaves and Sepals

We considered the first stages of leaf and sepal development, when asymmetry is set up and the organs start to grow out along the three axes. *Arabidopsis* leaves were studied from initiation until 5 days after initiation (5 DAI, as described in [9]). Sepals were monitored until floral stage 6, when the organs have covered the floral meristem (as defined in [15]). During these stages of development, both organs are readily accessible for live imaging. Tomato leaves were studied up to P_4, which is the fourth youngest primordium.

Primordia of leaves and leaf-like organs in both species initiate from apical meristems, as rounded, slightly asymmetric bulges (Figures 1 and S1). In the young leaf and sepal primordia, the ratio of blade width (in the mediolateral axis) to thickness (in the ad-abaxial axis) is between 1.5 and 2 where the primordium is the broadest. The leaf and sepal primordia mainly expand in 2D, forming eventually a thin lamina with final ratios of 10-12 in mature sepals and even higher in leaves [16] (Figures 1A, 1D, 5H, and S1).

From a mechanical point of view, growth directions largely rely on the orientation of the cellulose microfibrils in the cell walls [13, 14], which usually depends on the organization of the cortical microtubule (CMT) arrays guiding the cellulose synthase complexes [18]. To investigate the role of CMTs in leaf development, we first characterized their arrangements using immunostaining and *in vivo* confocal imaging (Figures 1B, 1E–1J, 1L, and 1M). In *Arabidopsis*, CMT behavior along the walls in the plane of the leaf blade was highly dynamic. In young growing sepals at stage 3/4, these CMTs showed a certain degree of anisotropy (Figures 1E and 1F, see also [19]), which decreased significantly from stage 5 onward (from 0.233 ± 0.071 to 0.114 ± 0.051, $p < 0.001$ by Student's t test) (Figures 1H–1I, and 1K [19]. Similarly, the young leaf also showed aligned CMTs along these walls until 1–2 DAI, but adopted highly variable arrangements afterward (Figure S2). This behavior was not only observed at the surface but also along walls parallel to the surface in the inner L1/L2 interface (drop of anisotropy by 46% in stage 5/6 sepals, from 0.142 ± 0.086 to 0.077 ± 0.046, $p < 0.001$ by Student's t test) (Figures 1L–1N).

A very stable behavior was found along most of the internal walls oriented in the ad-abaxial direction. Here, CMTs were mainly oriented perpendicular to the plane of the blade (i.e., in the ad-abaxial direction) in *Arabidopsis* cotyledons, leaves (at least until 5 DAI), and sepals (at least until stage 6), as well as in tomato leaves (at least until stage P_3) (Figures 1B, 1G, 1J, S2, and S3). Staining of cellulose confirmed that this coincided with the main microfibril orientation in these walls (Figures 1C and S3C), while the cellulose synthase-associated proteins followed paths along the CMTs in growing sepal epidermal cells in *Arabidopsis* (Figures S3D–S3I).

To further evaluate the role of CMTs in leaf development, we treated primordia in both *Arabidopsis* and tomato with the CMT-depolymerizing drug *oryzalin*, at concentrations at which primordia continued to grow. After the mock treatment, the width to thickness ratio increased by 44% (from 2.637 ± 0.029 to 3.808 ± 0.053, mean ± SD) after two days, which was similar to that of untreated leaves. After oryzalin treatment, the outgrowing leaves in both species and sepals in *Arabidopsis* were thicker, while lateral expansion was compromised (Figures 2A–2I). The width-to-thickness ratio in sepals was even slightly reduced (13% drop, from 2.652 ± 0.035 to 2.304 ± 0.103) (Figures 2A–2G). At low concentrations (see STAR Methods), cells continued to divide, and division plane alignment became more variable (Figures 2J and 2K). This further confirmed that CMTs arrays are crucial for asymmetric leaf expansion.

CMTs Align along the Predicted Principal Axis of Stress in Specific Cell Walls

In plants, turgor pressure and differential growth both generate mechanical stresses within the cell walls [20], and CMTs often align with the predicted axis of maximal tensile stress [21, 22]. If this is also the case in the leaf, our observations of CMT orientations in leaves would suggest that the internal walls are experiencing highly anisotropic tensile stresses in the ad-abaxial direction. To calculate the stress patterns in flat organs and take into account the mechanical influence of all walls throughout the tissue in 3 dimensions (3D), we next used a computational modeling approach. For this purpose, we developed a finite element (FE), 3D multicellular model of a young leaf (adapted

(M) the L1/L2 wall interface of (I) shows isotropic CMTs.
(N) Quantification of CMTs in L1/L2 walls in the plane of the sepal blade at stage 3/4 and stage 5/6 using *Fibriltool* [17], showing a drop of degree of anisotropy as the development of sepals (n = 56 cells from 4 stage 3/4 sepals; n = 71 cells from 5 stage 5/6 sepals; $p < 0.001$ by Student's t test).
Scale bars, 20 μm (A)–(D); 10 μm (J)–(M). See also Figures S1–S3.

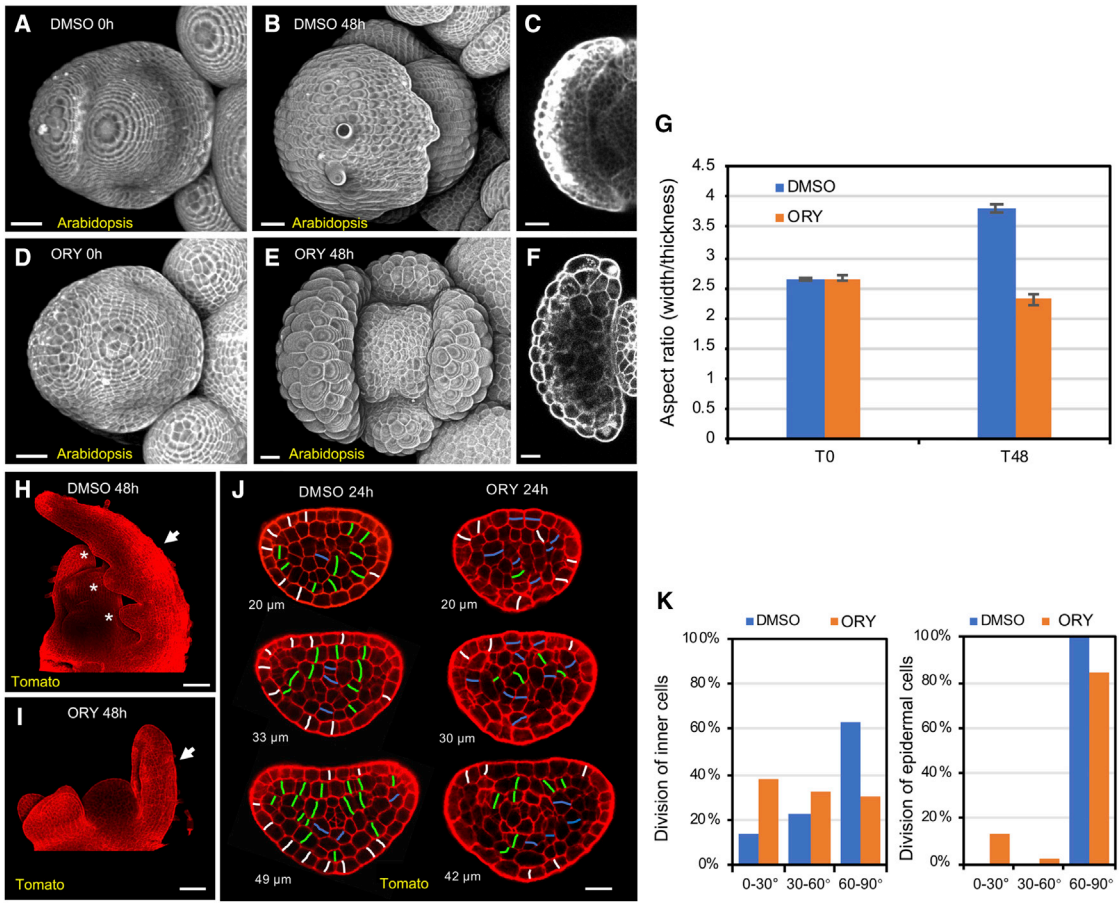


Figure 2. Oryzalin Treatment and Cell Division in Developing Leaves and Sepals

(A–F) *Arabidopsis* sepal development after the treatment of DMSO (A–C) or oryzalin (D–F) for 0 h (A and D) and 48 h (B, C, E, and F). Note that the growth continues after the oryzalin treatment. Cross sections of sepals in (B) and (E) are shown in (C) and (F).

(G) Quantification of width/thickness ratios. Treated sepals do not flatten (n = 3 biological repeats).

(H and I) The morphology of tomato P_2 48 h after the treatment with DMSO (H) or oryzalin (I). Arrows indicate the primordia treated with chemicals. Leaf primordium treated with DMSO show normal anisotropic growth and generate lateral leaflet primordia (asterisks). The anisotropic growth and planar leaf form are compromised in oryzalin treated samples.

(J) Cell division pattern by mPS-PI staining in optical cross sections of tomato P_2 treated with DMSO (left column) or oryzalin (right column) for 24 h. White, divisions perpendicular to the epidermis; blue, divisions parallel (angle < 30°) to mediolateral axis in inner cells or to the epidermis; green, other divisions (30° < angle < 90°).

(K) Quantification of cell division pattern in (J).

For DMSO treatment, n = 146 cells, and for oryzalin treatment, n = 91 cells. Scale bars, 20 μm in (A)–(F) and (J) 100 μm (H) and (I).

from [23]) see STAR Methods and Methods S1 for 3D model description), inflated by a steady and uniform pressure. Incipient leaves were represented as ellipsoidal shapes with alveolate structures composed of about 800 cells. This is in the same order of magnitude as, for example, the very young sepal primordia *in vivo*, which can be considered as half ellipsoids containing about 150–200 cells (our unpublished results). The number of FEs per cell wall was about 10–20 (Figure 3A). We used aspect ratios comparable to that of young primordia (Methods S1). *In vivo*, the outer walls of the growing leaves were about 3 and 4 times thicker in *Arabidopsis* and tomato leaves, respectively (Figure S4). These differences have been interpreted in terms of differences in stiffness (e.g., [24] and references therein). Therefore, the outer walls were made 3 times stiffer than the inner walls in the model.

When this structure was put under tension, the maximal stress in the internal walls was in the ad-abaxial direction (i.e., along shortest axis of the ellipsoid, Figure 3C). At the outer surface, wall strain and stress were mainly aligned mediolaterally (transversely) with respect to organ shape, (i.e., along the second axis of the ellipsoid, Figure 3D). These results therefore confirm that CMTs align along the main predicted force directions at early stages of leaf (up to 1–2 DAI) and sepal (up to stage 3/4) development. At later stages, the leaf and sepal shapes are roughly still ellipsoidal, and the dominant stress directions remained unchanged. From stage 5 onward, the observed CMTs continued to align with the predicted stress in internal tissues (Figures 1J, 3B, and 3C). However, they were no longer aligned with the predicted orientation of the main stress in the outer surface walls (Figures 1H–1I, Figures 3B and 3D).

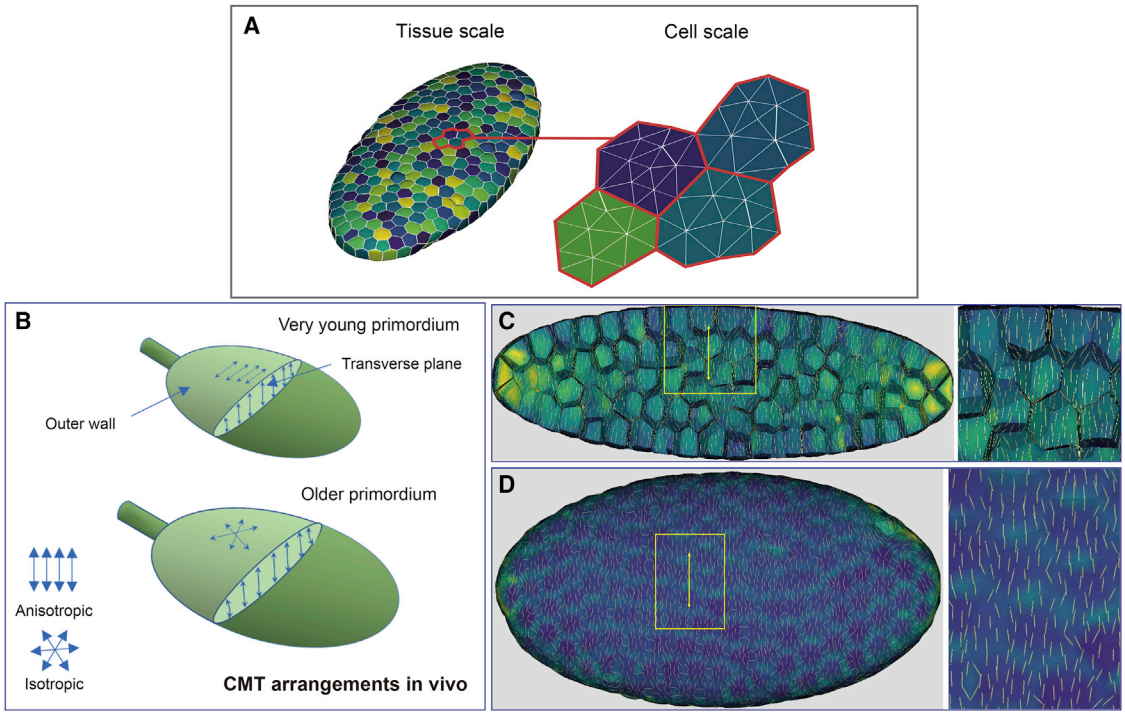


Figure 3. CMTs Align along Predicted Force Patterns

(A) Overview of the 3D mechanical model. Virtual tissues with outer and inner cell walls are composed of triangular finite elements (see Methods S1 for details).

(B) Summary of observed *in vivo* CMT patterns described in Figure 1. CMTs on the outer wall adopt variable arrangements, while the inner walls in the ad-abaxial direction systematically show CMTs in the ad-abaxial direction.

(C) Simulation (overview and detail) showing the predicted main force directions (yellow double arrow) in internal walls of the ellipsoid put under pressure. Inside, the dominant forces run along internal the ad-abaxial axis.

(D) Surface view (overview and detail) of the same simulation showing the main force directions (yellow double arrow) along the mediolateral axis. See also Figures S4 and S5.

Exploring Mechanical Feedback as a Possible Mechanism Involved in Leaf Morphogenesis

To explain the coordinated alignment of microtubules throughout tissues, a range of studies have suggested the existence of a mechanical feedback mechanism that coordinates CMT alignment [21]. It has been proposed that the cells can sense the main force direction along each individual wall and orient their microtubules parallel to this direction. This would in turn lead to the CMT-guided deposition of cellulose microfibrils and wall reinforcement restricting growth in the orientation of maximal tension (Figure 4A). Although a molecular mechanism for directional stress sensing has not been identified, a strong correlation between stress directions and CMT alignments has been reported in several tissues, including shoot apical meristems, stems, and hypocotyls [22, 25–27]. In leaves and sepals, CMTs stictly align with the predicted stress in internal tissues (Figure 3B), which is compatible with mechanical feedback along these walls. On the other hand, there is a temporal discrepancy between the predicted stress orientations and the observed CMT orientation at the surface of older leaves and sepals, suggesting modulation of the mechanical feedback at the surface. Is the mechanical feedback along internal walls necessary for flattened shapes? Is a modulated mechanical feedback on the surface compatible with growth dynamics leading to leaf flattening? Is there any experimental evidence for such a selective coordination of CMT alignment?

To address these questions, we first investigated whether this mechanical feedback could provide, on theoretical grounds, a plausible scenario for leaf morphogenesis. We therefore introduced pressure-driven growth in the aforementioned 3D structures, as detailed in [11], based on a multidimensional extension of Lockhart's strain-based growth model [10] to simulate 3D multicellular tissues. This can be summarized as follows. Plant cells are under high pressure, which, in a non-growing isolated cell, is counterbalanced by tension in the extracellular matrix or cell wall. If this pressure exceeds a certain threshold, the load-bearing parts of the cell wall yield, and growth occurs. In addition, we simulated stress-based feedback on wall remodeling as described in [23] (see Methods S1). Briefly, the local material properties of the cell wall were represented by a fibrous material [28], parameterized by the directional density of microfibrils, considered as short linear elastic elements. In turn, these elastic properties were computed dynamically as an emergent property of stress through CMT reorientation and CMT-guided cellulose synthesis, which are explicitly modeled. It is technically not yet possible to take into account cell divisions in these 3D simulations. In addition, since remeshing was not possible, longer simulation times caused important deformations of the finite elements, causing numerical artifacts. Therefore, we analyzed

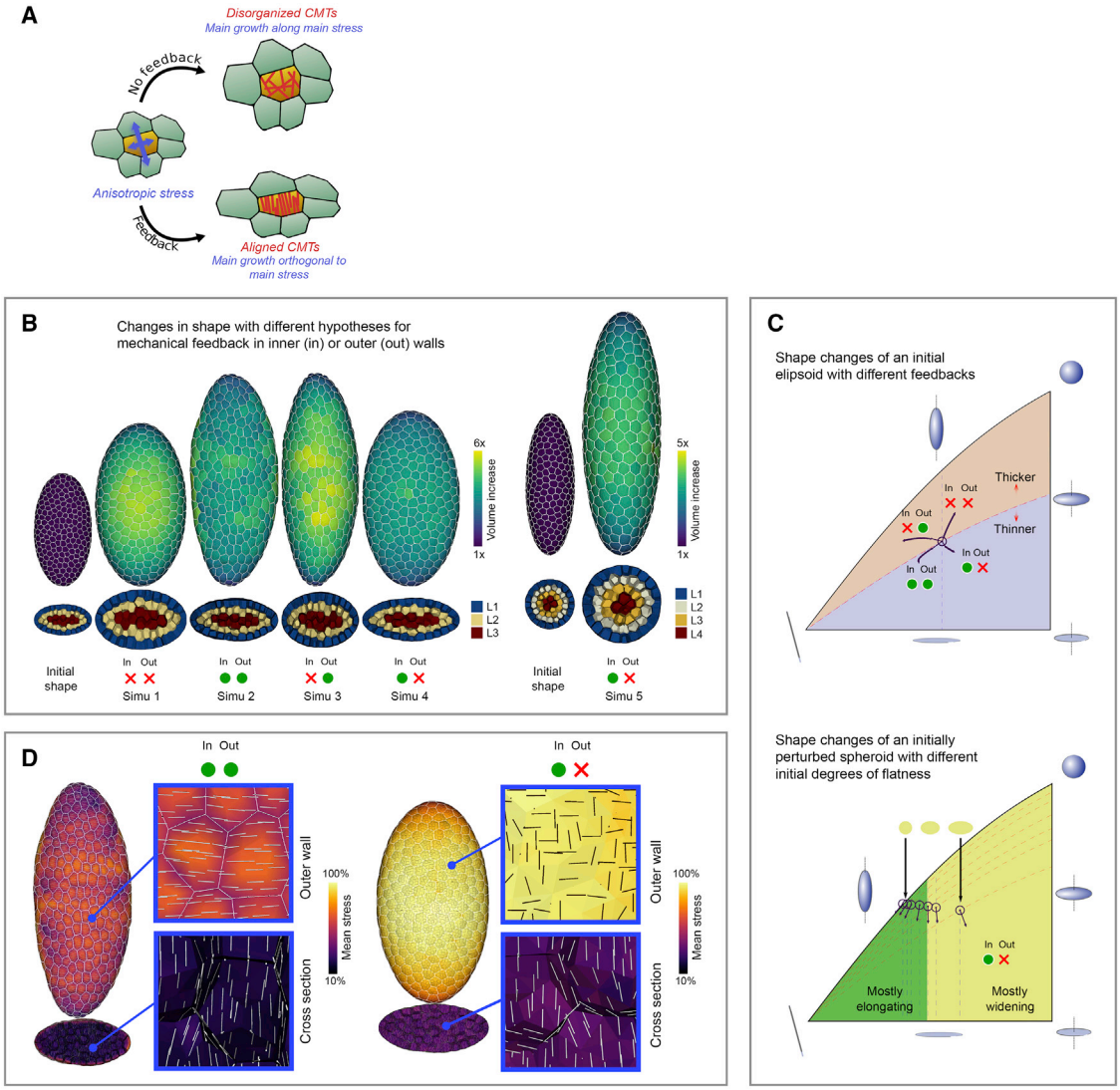


Figure 4. Computational Modeling

(A) Cartoon showing the basic principle of the mechanical feedback. If this mechanism is activated, the microtubules will align along the main force direction in an anisotropic force field and inhibit growth in that direction via the deposition of cellulose microfibrils (blue arrows: minimal and maximal force direction according to arrow length).

(B) Outcome of five different scenarios. Starting from a flattened ellipsoid (simulations [simu] 1–4), different levels of flatness amplification can be achieved, depending on whether the feedback is active (green dot) or inactive (red cross) on outer and/or inner walls. Without feedback (simu 1), the structure becomes rounder. With feedback everywhere (simu 2), the structure becomes longer (and slightly flatter). With feedback on the outside only (simu 3), the structure becomes thicker and grows toward a cylindrical shape. Maximal flattening is obtained with feedback on inner walls only (simulation 4). A spheroid (simu 5) remains axisymmetric with the same feedback on inner walls only.

(C) Upper diagram: ellipsoids shape changes. These can be represented as respectively points and trajectories on a 2D diagram (see Methods S1). Feedback in the inner tissues causes flattening (trajectories below the dotted line). Lower diagram: in perturbed spheroidal structures, elongation largely dominates (trajectories in green area).

(D) Predicted CMT orientations in simulation 2 (left panel) and 4 (right panel). Both simulations predict anisotropic CMTs along walls in the ad-abaxial direction as observed *in vivo* (see white line segments on cross sections). Simulation 2 systematically leads to highly anisotropic CMTs/cellulose microfibrils on outer walls (white line segments on outer wall), which is not always observed *in vivo*. See also Videos S1, S2, S3, and S4.

the impact of the feedback loop for a period no longer than a threefold change in volume (i.e., 1–2 cell cycles), where these limitations were not problematic.

Without mechanical feedback, the virtual structure evolved toward a spherical shape in view of the resulting strain field (simulation 1: Figures 4A and 4B; Video S1). This qualitatively echoes the results obtained *in vivo* using oryzalin treatment. When the stress feedback was active throughout the entire 3D tissue, the structure grew longer (and slightly flattened), showing that at least over short time periods, a stress feedback has the potential to not only maintain but also promote anisotropic expansion (simulation 2: Figures 4B and 4C; Video S2, outer and inner

feedback active). In line with the experimental evidence, these simulations showed CMT alignment along the ad-abaxial axis (Figure 4D, left panel), restricting an increase in thickness. However, they also systematically predicted a mediolateral alignment of CMT arrays along the stiffer outer surface walls (Figure 4D, left panel), which is not seen *in vivo*. In addition, we observed, *in silico*, that the CMTs along the outer and inner walls parallel to the leaf blade became oriented perpendicularly to each other (Figure S5A). This pattern created a mechanical conflict that perturbed growth during longer simulations. In addition, we did not observe such antagonist CMT orientations in leaves and sepals *in planta*, either. This mechanical conflict observed *in silico* probably resulted from the stress responsive reaction of inner tissues that tend to oppose to the apical-basal expansion of the outer wall, which is itself promoted by the stress-based feedback.

Since, *in vivo,* CMTs at the surface no longer align with the predicted force directions from certain stages onward (Figures 1H–1I, S2C–S2E, and S2G–S2I), we next performed simulations where the CMT feedback was inactivated there. We reasoned that this downregulation would lessen the mechanical conflict, while presumably not changing the main stress orientations in the inner layers. In simulations where the stress feedback on CMT orientation was inactivated at the outer surface walls, the mechanical conflict was indeed eliminated, causing even further amplification of organ flatness (simulation 4: Figures 4B and 4C; Video S4). Importantly, the arrangements of CMTs along the surface and along all inner walls were consistent with the *in vivo* observations on sepals at floral stage 5 and leaves at 2 DAI (Figure 4D, right panel; Figure S5B). Therefore, a downregulation of the feedback mechanism in the outer surface walls was sufficient to restore the consistency of the simulations with the observations made on leaves and sepals at later stages. Note that, by contrast, activating mechanical feedback at the outer walls only, resulted in reduced asymmetry as the virtual organ developed toward an axisymmetric elongated shape (simulation 3: Figures 4B and 4C; Video S3).

The predicted mechanical feedback along the outer surface walls was tested using *katanin* (*ktn*) mutants. KTN is involved in microtubule rearrangement, and its mutation leads to delayed CMT response to stress [29–31] In *ktn* mutants, CMT arrays are isotropic under low stress levels but behave similar to wild-type plants under high levels. Different from wild-type leaves and sepals, the *ktn* mutants *bot* and *lue1* showed lower degrees of CMT anisotropy at their surface even during the youngest stages (Figures 5A–5C, compared with Figure 1K). On the other hand, the CMTs in the ad-abaxial direction and derived cellulose microfibril deposition remained strictly aligned, as in the wild type (Figures 5D–5G). This indicates that in the *ktn* mutants the CMTs on the outer surface wall never align with the predicted stress patterns, in contrast to the inner, ad-abaxially oriented walls. Consistent with our simulations, the mutant leaf and sepal blades were relatively wider, while maintaining thickness at wild-type levels (Figures 5H–5J).

Contribution of Cell Divisions to Directional Blade Growth

In addition to the reinforcement of ad-abaxial walls along stress patterns, leaf flatness could in principle be further enhanced through cell division plane alignment in the same direction. It is known that cells often divide in a plane parallel to the microtubule interphase array [32, 33]. Accordingly, we observed that the division planes were mostly perpendicular to the plane of the leaf blade in the epidermis and L2 layers (Figures 2J–2K and S6). Such anticlinal walls should in principle further increase the resistance of the tissue to thickening, and thus, both cellulose deposition and the orientation of new cross walls would contribute synergistically to the final leaf shape. Since, as mentioned previously, 3D modeling frameworks are not yet able to support realistic 3D cell division, we designed a 2D model to test the potential contribution of cell divisions to flattening in a cross section through the leaf (see STAR Methods and Methods S2; Figure 6).

The 2D model integrates a stress-based feedback loop that regulates the cell wall stiffness of the inner walls as a function of wall tension (see STAR Methods). In view of the results described above, we implemented a feedback, where only the inner walls stiffened in response to the main forces that were acting on the cell. Without division, the feedback on wall stiffening alone initially caused a flattening, which was not maintained in long-term simulations (Video S5). This is because no new cell walls were added to compensate for the increasing surface, which in the long run overrides the feedback. Note that in contrast to the 3D model, the 2D model cannot take into account the in-plane walls. There might be ways to compensate for this, but that would complexify the model, which is not necessary, as its main purpose was to investigate the role of oriented divisions.

We next performed simulations, including cell division. The precise mechanisms that establish specific division planes are still under debate. We therefore used simple rules that would qualitatively reproduce the observed patterns (Figures 2J–2K and S6).

(1) For the epidermis, we simply imposed the observed behavior *in vivo*; i.e., the cells divided perpendicular to their outer surface (Figures 1K and S6G–S6H).
(2) For the internal cells, with no outer surface, we tested several alternative scenarios described in the literature (see Methods S2).

In vivo, cells in the internal layers divide in more variable directions but tend to divide preferentially at an interval of 60°–90° to the mediolateral axis of the leaf primordium (Figures 1K, S6E, and S6F). We were able to recapitulate the observed internal cell division patterns when these cells were instructed to divide along the main tensile stress directions (as in [34]). Applying these division rules for epidermal and internal cells clearly showed the effect of cell division on further flattening of the ellipse (Figure 6; Videos S5, S6, and S7). Although the model is mainly designed to provide qualitative information, we noted that the aspect ratio (width/thickness) during this simulation increased from 1.75 to 2.5 for a five-fold increase in the cross-sectional area. This is in the same order of magnitude as what is observed *in vivo* during early leaf development (from around 1.7 to 2.6 for a five-fold increase in the cross-sectional area, see Figure 6). We also tested a scenario where all new walls were randomly oriented. In that case, the structure was able to maintain its initial aspect ratio but failed to flatten more (Video S6).

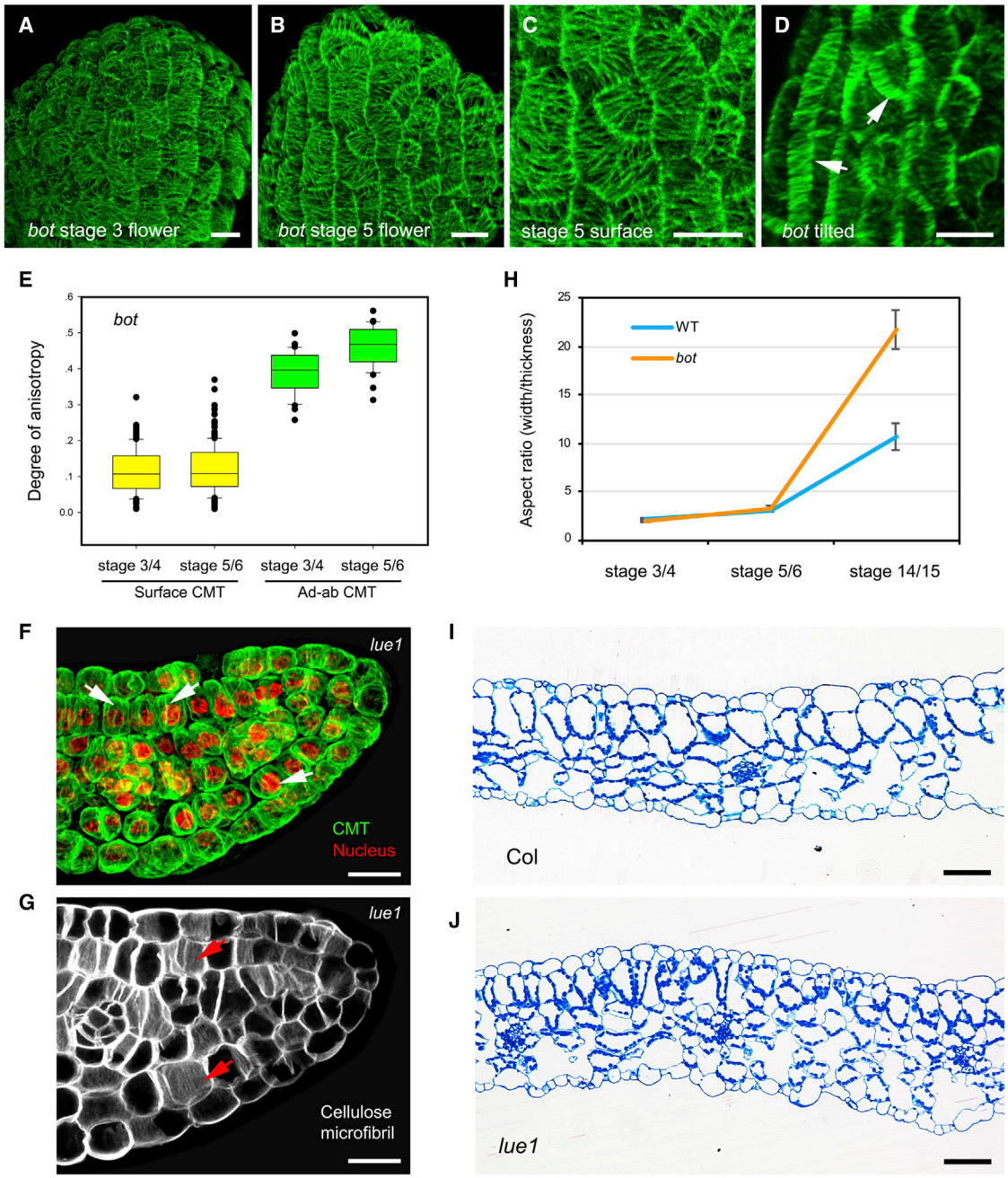


Figure 5. CMT and Cellulose Microfibril Arrangements in *ktn* Mutants

(A and B) Overview of a stage 3 (A) or a stage 5 (B) *bot* flower bud expressing GFP-MBD showing isotropic CMTs on the outer surface.

(C) Detail showing random orientation of CMTs along the sepal surface in (B).

(D) Tilted detail of (B). CMTs along the ad-abaxial direction remain highly anisotropic in *bot* (indicated by arrows).

(E) Quantification of CMT orientations using *Fibriltool* [17]. Wild-type sepals at stage 3/4 have a higher degree of anisotropy on their outer walls than at stage 5/6 (see Figure 1K), while in *bot* mutant, anisotropy is low from early stages onward. By contrast, CMTs on walls in the ad-abaxial direction remain highly anisotropic throughout development. n = 100 cells from 4 stage 3/4 sepals, and n = 255 cells from 7 stage 5/6 sepals for analysis of surface walls; n = 31 walls from 3 stage 3/4 sepals, and n = 36 walls from 4 stage 5/6 sepals for CMTs in the ad-abaxial direction.

(F) Immunostaining of CMT organization (green) with nuclei stained by DAPI (red) in cross sections of *lue1* leaf primordia. CMTs on walls in the ad-abaxial direction are anisotropic, as indicated with white arrows.

(G) Cellulose microfibrils stained by Direct Red 23 (white) in cross sections of *lue1* leaf primordia are anisotropic in the ad-abaxial direction, as indicated with red arrows.

(H) Quantification of width/thickness ratios in Col-0 and *bot* sepals. n = 10 Col-0 and 7 *bot* sepals at stage 3/4. n = 9 Col-0 and 11 *bot* sepals at stage 5/6. n = 11 Col-0 and 8 *bot* sepals at stage 14/15.

(I and J) Cross sections of mature leaves of Col-0 wild type (I) and *lue1* (J) showing comparable thickness.

Scale bars, 10 μm (A)–(D); 5 μm in (F and G); 50 μm (I) and (J).

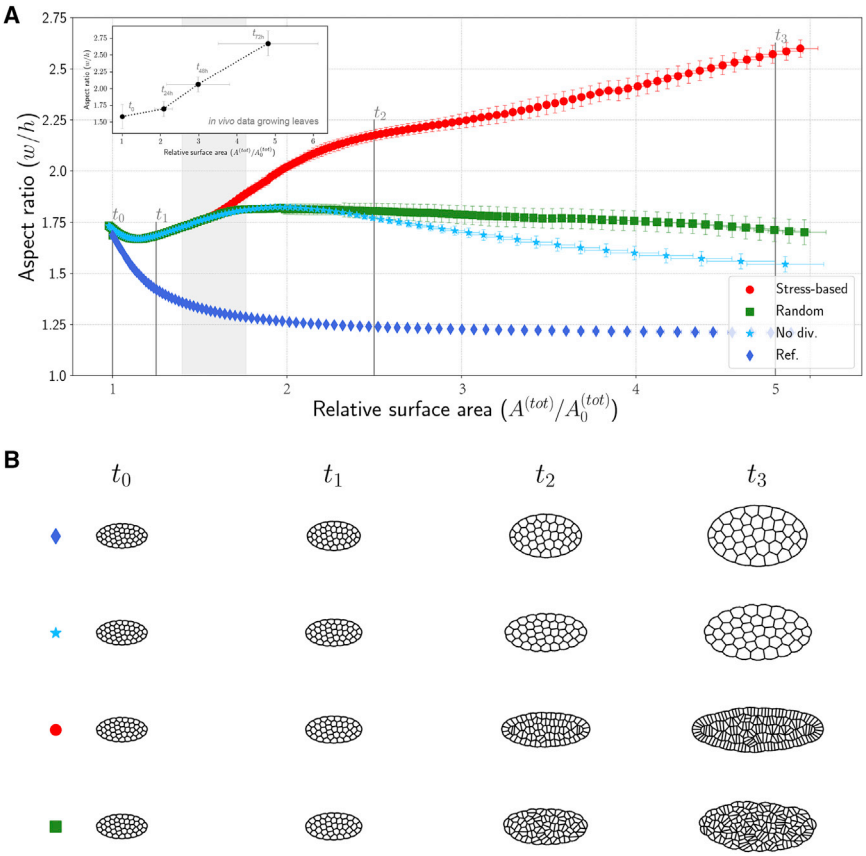


Figure 6. The Effect of Cell Division on Leaf Flattening Using 2D Modeling

(A) Quantified aspect ratios (width over height) in growing 2D structures as a function of their relative surface areas. Each set of simulations is composed of ten replicates in which the same parameter values are used, but each simulation is run on a variant of the same initial structure (see Methods S2). The coordinates of each point correspond to the median values of the corresponding geometrical variables computed over ten replicates. The error bars depict the one and three quarter percentiles of the value distribution over the replicates. All the curves do not feature the exact same amount of points for they did not develop at the same speed.

The four main scenarios are shown: (1) growth without mechanical feedback and without cell division (marked by blue diamonds), see Video S5; (2) growth with feedback and no cell division (marked by light blue stars) after an initial flattening, the structure starts to thicken again as stresses increase and override the feedback, see Video S5; (3) feedback and randomly oriented divisions everywhere (green squares) showing increased flatness when compared to the previous scenario, see Video S6; (4) growth with both feedback and oriented cell divisions (red circles), see Video S7. In the latter case, division planes in the L1 are all perpendicular to the surface; inner cells divide parallel to the main stress direction. This scenario results in a clear flattening. The indicated time points ($t_{0\text{-}3}$) correspond to the initial state (t_0), the situation at the beginning of first wave of the cell divisions (t_1), the situation just before the second wave of cell divisions (t_2), and the situation at 150 simulation steps (t_3).

Inset in (A) represents the quantification of aspect ratios (width over height) in *Arabidopsis* leaf primordia as a function of their relative areas of cross section. Measurements have been performed from 5 different leaf primordia. The initial state (t_0) corresponds to the leaf primordia at around 1DAI. Growth was recorded every 24 h and for 72 h in total. Error bars correspond to the standard deviation from the mean value.

(B) Visual outputs of the same simulations as in (A). The represented outputs correspond to the initial shape (corresponding to time point t_0 in (A), intermediate steps (t_1 and t_2), and the shape after 150 simulation steps (t_3). The diamond, star, square and circle correspond to the symbols used in (A). See also Figure S6 and Videos S5, S6, and S7.

Together, these results point at the importance of adding new mechanical elements in the form of cell walls in particular directions to further promote flattening.

The Role of the Margin Genes in Defining Organ Shape

We next investigated CMT alignment in mutants defective in leaf flattening. As mentioned above, WOX1 and PRS are two transcription factors expressed at the leaf margin and middle domain, and a double *wox1 prs* knockout has reduced margin activity, slightly narrower leaves, and a clear reduction in sepal width (compare Figures 7A and 7B). This phenotype is enhanced when *wox1 prs* is combined with a third mutation, *as2*, which has (nearly) axisymmetric sepals (Figures 7C and 7D) and leaves [4].

Imaging GFP-MBD revealed highly anisotropic CMT arrays along the inner anticlinal walls (i.e., perpendicular to the surface) of *wox1 prs as2* sepals and leaves (Figures 7G and 7J). Variable CMT arrangements were found along the surface of radialized young primordia: isotropic in leaves and highly anisotropic in sepals (Figures 7E–7F, 7H, and I). Highly anisotropic CMTs were also found in *wox1 prs* sepal primordia, which have a weaker phenotype (Figures S3J and S3K). This indicates that CMTs keep the arrangements also found in wild-type plants and suggests that the margin genes and polarity genes are not required for the coordination of CMT organization. The results in *Arabidopsis* were further confirmed using microsurgery in tomato. Isolation of an incipient leaf primordium from the meristem using ablation results in compromised *WOX* expression, leaf margin formation, and flattening [5]. Both CMT arrays and cellulose microfibrils showed anisotropic arrangements in these (nearly) axisymmetric leaves (Figures 7K–7N). Together, these results suggest that the margin genes act independently from CMTs in leaf flattening.

It has been proposed that *WOX1* and *PRS* promote cell proliferation at the leaf margin, thus causing broadening of the leaf blade [4, 35]. In addition, we identified a very early phenotype in the corresponding mutants. In flowers, the sepals of the double *wox1 prs* mutant are narrower from early stages (stage 4) onward (Figure 7R), while the boundaries between them are enlarged (Figure S7). This is consistent with the onset of *PRS* expression in leaf primordia prior to primordium formation [36, 37]. This very early phenotype was further enhanced in the triple *wox1 prs as2* knockout. Soon after initiation (Figure S7), the

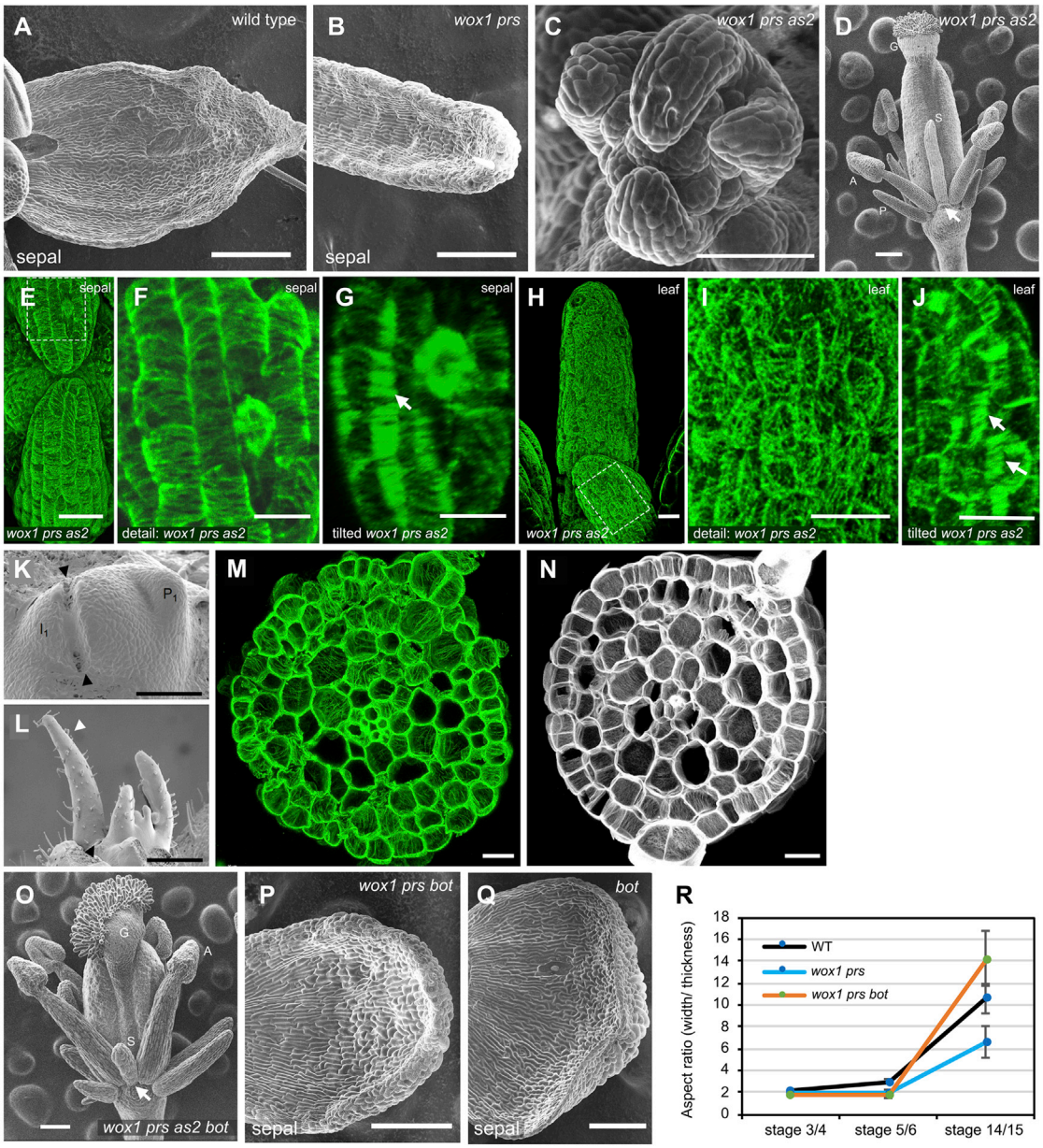


Figure 7. CMT and Cellulose Microfibril Arrangements in Polarity Mutants and Effect of *ktn*

(A and B) Sepal phenotypes in wild type (A) and *wox1 prs* (B).

(C) Axisymmetric sepal primordia with increased boundary domains in *wox1 prs as2*.

(D) Axisymmetric organs (overview) in a flower bud of the triple *wox1 prs as2* mutant.

(E–J) Overview of phenotype and CMT alignment in a finger-like sepal (E–G) and a leaf (H–J) of *wox1 prs as2.*

(F and I) Details of (E) and (H) showing anisotropic (F) and random (I) CMT arrangements on walls at the surface of the leaf blade, respectively.

(G and J) tilted detail of (F and I) showing anisotropic CMTs in the ad-abaxial directions, respectively.

(K–N) Isolation of an incipient leaf primordium in tomato from the meristem results in the formation of axisymmetric leaves (K and L). CMTs (M) and cellulose microfibrils (N) are mostly oriented in ad-abaxial directions in cross sections.

(O) Quadruple *wox1 prs as2 bot* mutant organs remain close to axisymmetric.

(P and Q) Sepal phenotype in *wox1 prs bot* (P) and *bot* (Q).

(R) Quantification of width/thickness ratios, showing that *bot* increases width in the double mutant. Note that there is still some margin identity left. n = 10 wild type, 7 *wox1 prs*, and 8 *wox1 prs bot* sepals at stage 3/4. n = 9 wild type, 9 *wox1 prs*, and 8 *wox1 prs bot* sepals at stage 5/6. n = 11 wild type, 10 *wox1 prs*, and 8 *wox1 prs bot* sepals at stage 14/15.

Abbreviations in (D and O): S, sepal; P, petal; A, anther; G, gynoecium. Scale bars, 100 μm in (A, B, D, O, K and L); 50 μm in (C); 20 μm in (E, H–J, M, N); and10 μm in (F–G). See also Figure S7.

primordia became almost axisymmetric, and the boundary domains were even further enlarged. The sepals then mainly grew in the apical-basal direction (Figures 7C and 7D). We thus conclude that *WOX1* and *PRS* convert the very early leaf primordium into a flattened ellipsoid-like shape, probably by promoting margin cell proliferation, but not affecting the coordination of CMTs. This also raised the question of to what extent the initial shape of the primordium contributes to its final shape.

To better understand the potential impact of an initial degree of asymmetry on stress-based organ flattening, we used our 3D modeling framework to further investigate the system's dynamics in the organ morphospace. We thus focused our exploration on short trajectory segments using ellipsoids with various degrees of initial flatness to analyze trends in shape deformation. Starting from elongated ellipsoids close to axisymmetry, we found that the degree of stress-driven flattening depended not only on the activation of the feedback itself but also on the initial degree of shape asymmetry: the flatter the initial structure, the more rapidly it flattened (Figure 4C, lower panel). This suggested a scenario in which the margin genes promote the formation of a flattened initium and thus provide, in conjunction with the coordination of CMT alignment, the mechanical conditions for further flattening of the leaf blade.

The simulations with mechanical feedback starting from nearly axisymmetric structures mainly elongate, and flattening was negligible (Figure 4C, lower panel). A perfectly axisymmetric structure maintained itself as such, because the feedback mechanism is on its own not able to break the axisymmetry (simulation 5: Figures 4B and 4C, lower panel). This would correspond to mutants like *wox1 prs as2* in which margin activity is completely impaired and sepals or leaves mainly elongate and do not flatten. These mutants are in a different regime, and modulating CMT alignment using *bot* was not able to induce significant flattening: sepals remained close to axisymmetric in *wox1 prs as2 bot* (Figure 7O). This is in contrast to the effect of inactivating KTN when the margin activity is only partially impaired: in the *wox1 prs* background, *bot* still promotes flattening (Figures 7P–7R).

DISCUSSION

Our results lead to a scenario in which CMT alignment along the main stress directions in the ad-abaxial direction contributes to the control of blade formation. Since CMTs align along the direction of the main tensile stress in several tissues, including meristematic tissues, roots, and stems, a feedback mechanism has been proposed, in which cells directly use mechanical cues to organize their CMTs. We show here that the observed CMT alignments along walls in the ad-abaxial direction in leaves can in principle be achieved using such a stress-based feedback. This was also proposed for the microtubule arrays on the surface of sepals during early development [19]. However, CMT alignment along these periclinal walls is more variable, suggesting a modulation of the mechanism, which in turn can modulate growth directions in the leaf blade.

The molecular mechanism behind the tissue-wide coordination of CMT orientation remains elusive [21]. Although we focus here on mechanical cues, the link between stress and the cytoskeleton could be largely indirect. Chemical gradients along the ad-abaxial axis, for example, could be involved in orienting the CMTs. In that case, CMTs would subsequently orient the cellulose microfibrils along such gradients, restricting the thickening of the leaf and maintaining the main force directions in the ad-abaxial direction. Although chemical gradients between the ad-abaxial sides of the leaf have been described [2, 3], a gradient controlling CMTs has not been identified. Note that even in the *wox1 prs as2* mutant in which ad-abaxial polarity is impaired and the corresponding biochemical gradient is absent, CMTs remain highly aligned. Whatever the mechanism, the orientation of CMTs along the main, internal stress directions has the potential to both amplify bilateral asymmetry during leaf development and promote the elongation of axisymmetric organs. This is a robust property, which is reproduced in our model with a minimum of hypotheses. It is important to note that the outcomes of our simulations are mainly qualitative in nature. It is therefore not possible at this stage to predict with precision to what extent the CMT alignments contribute to the final flatness or to what extent any CMT orienting mechanism would contribute. A limitation lies in the absence of cell division, which imposes short simulation periods. To nevertheless provide an indication, we performed simulations with different cell numbers. The higher the cell number, the larger the structure was, which mimicked the effects of cell division (Figures S5E and S5F). As *in vivo*, the larger structures were also flatter. This again strongly suggested that with increased cell number and volume, the mechanical feedback had the potential to induce continuous flattening.

Our models were not designed to reproduce later stages of leaf development, when cell division ceases and cell volume increases. Even at constant pressure, wall tension will increase with increasing volume and changing curvature, as dictated by Laplace's law. This causes the ellipsoid to thicken during longer simulations, as the cells become too big and the increasing forces override the feedback mechanism. *In vivo*, a plant has to face the same problem. It has several means to deal with this. As we show here, cell division is one way. When cell division ceases, other means could involve further anisotropic reinforcement of the walls or reducing pressure. Recent work has also suggested that the anisotropic arrangement of matrix molecules, such as pectins, could play a role in more mature cells [38]. Finally, it is important to note that the physical status of the leaf later on during development might be very different, as the cells become separated by air spaces. However, we do not know anything about these later dynamics and preferred not to include further hypotheses, and we wanted to keep the models as simple as possible. By any means, to remain flat during growth, the walls have to be highly anisotropic.

Our results also point at additional layers of regulation. First, CMTs at the surface do not align systematically along the predicted force directions. This could have different explanations. The higher stiffness of the outer wall might make the underlying membranes less sensitive to stress, for example. Alternatively, polar localized proteins might affect the ability of CMTs to align properly along the surface. It is also possible that *in silico* predictions diverge from *in planta* stress patterns, which can be attributed to nonuniform turgor pressure and/or other mechanical properties, which we cannot reliably measure yet. A second layer of regulation involves the margin and polarity genes. We propose

that these genes are not required for the coordinated behavior of microtubules but rather define an initial degree of primordium flatness, which then can be amplified by CMT-based growth anisotropy. In addition, these genes might contribute to leaf flatness later on during primordium development. *WOX1* and *PRS* are able to promote cell division. Indeed, their ectopic expression in the adaxial or abaxial sides can lead to increased leaf thickening or the formation of ectopic rounded protrusions accompanied by increased cell proliferation [4, 35], but not ectopic blades. By promoting cell proliferation at the margin, they promote leaf blade flattening in combination with the CMT-based mechanical feedback.

In vivo, perfectly axisymmetric lateral organs do not exist. If the mechanical feedback indeed operates, this would imply that all organs should be flattening if growth was infinite. However, this flattening could be extremely limited: *in silico,* nearly axisymmetric structures flatten very slowly and mainly elongate in the apical-basal direction, resulting in the formation of finger-like shapes (simulation 5: Figures 4B and 4C). We would therefore expect that the flattening of nearly axisymmetric structures would not be visible *in vivo*. In addition, further regulation, e.g., including activation of the feedback on the outer walls of the epidermis could further stabilize axisymmetry. In roots, for example, microtubules along the outer walls of the epidermis in the elongation zone are highly anisotropic and could thus contribute to the cylindrical shape of the organ (e.g. [39]).

The flattened unifacial leaves of *Juncus prismatocarpus* have blades along the ad-abaxial axis but not the mediolateral axis, suggesting that blade formation can be independent of ad-abaxial polarity establishment. The unifacial leaves lack adaxial identity and have *PRS* orthologs expressed in the margin-like regions along the ad-abaxial axis [40]. This suggests that the initial ad-abaxial asymmetry is amplified to obtain a leaf blade along the ad-abaxial axis, even when there is no adaxial identity. The stems of several phyllogenetically distinct plants are flattened, which are termed phylloclades. Furthermore, a plant may be composed entirely of flattened stems or of both cylindrical and flattened stems. The stress-based alignment of CMTs can be a unified underlying mechanism that amplifies any existing asymmetry.

STAR★METHODS

Detailed methods are provided in the online version of this paper and include the following:

- KEY RESOURCES TABLE
- RESOURCE AVAILABILITY
  - Lead Contact
  - Materials Availability
  - Data and Code Availability
- EXPERIMENTAL MODEL AND SUBJECT DETAILS
  - Growth conditions
- METHOD DETAILS
  - Visualization of microtubules
  - Oryzalin treatment
  - Agarose gel sectioning
  - Modified pseudo-Schiff-PI (mPS-PI) staining
  - Confocal microscopy
  - Image processing and analysis
  - Microsurgery and scanning electron microscopy
  - Cre-loxP based cell lineage tracing analysis
  - Semi-thin sectioning
  - Cell wall thickness measurement
  - Model description
- QUANTIFICATION AND STATISTICAL ANALYSIS

SUPPLEMENTAL INFORMATION

Supplemental Information can be found online at https://doi.org/10.1016/j.cub.2020.07.076.

ACKNOWLEDGMENTS

The authors would like to thank Olivier Hamant for reviewing the manuscript, Guillaume Cerutti for technical support, and Thomas Laux, Ari Pekka Mähönen, Ben Scheres, ABRC, and NASC for providing seeds. F.D., Q.W., and Y.J. were funded by the National Natural Science Foundation of China (NSFC) grants 31825002 and 31861143021, CAS Key Research Project of the Frontier Science (grant ZDBS-LY-SM012), and CAS PIFI grant 2020DB0001. Y.J. is a Newton Advanced Fellow of the Royal Society. J.T., F.Z., and W.C. were supported by the ERC advanced grant MORPHODYNAMICS (grant number 294397). J.T. and F.Z. were also funded by the ANR ERA CAPS grant Gene2Shape. J.T., C.G., O.A., and H.O. were supported by the Inria Project Lab "Morphogenetics." S.F. was supported by NSFC grant 11972200.

AUTHOR CONTRIBUTIONS

J.T., Y.J., and C.G. designed the research. F.Z., F.D., W.C., Q.W., R.S., and A.S. performed the experiments and analyzed the data. H.O., O.A., and C.G. designed and performed 3D modeling. L.Z., O.A., C.G., S.F., S.L., and M.L. designed and performed 2D modeling. J.T., C.G., Y.J., F.Z., F.D., and H.O. wrote the manuscript with inputs from all authors.

DECLARATION OF INTERESTS

The authors declare no competing interests.

Received: January 31, 2020
Revised: July 10, 2020
Accepted: July 27, 2020
Published: September 10, 2020

REFERENCES

1. Sachs, J. (1874). Traité de botanique conforme à l'état présent de la science. In Trad sur la 3, V. Tieghem, ed. (Savy).
2. Maugarny-Calès, A., and Laufs, P. (2018). Getting leaves into shape: a molecular, cellular, environmental and evolutionary view. Development *145*, dev161646.
3. Kuhlemeier, C., and Timmermans, M.C.P. (2016). The Sussex signal: insights into leaf dorsiventrality. Development *143*, 3230–3237.
4. Nakata, M., Matsumoto, N., Tsugeki, R., Rikirsch, E., Laux, T., and Okada, K. (2012). Roles of the middle domain-specific *WUSCHEL-RELATED HOMEOBOX* genes in early development of leaves in *Arabidopsis*. Plant Cell *24*, 519–535.
5. Shi, J., Dong, J., Xue, J., Wang, H., Yang, Z., Jiao, Y., Xu, L., and Huang, H. (2017). Model for the role of auxin polar transport in patterning of the leaf adaxial-abaxial axis. Plant J. *92*, 469–480.
6. Whitewoods, C.D., Gonçalves, B., Cheng, J., Cui, M., Kennaway, R., Lee, K., Bushell, C., Yu, M., Piao, C., and Coen, E. (2020). Evolution of

carnivorous traps from planar leaves through simple shifts in gene expression. Science *367*, 91–96.

7. Rebocho, A.B., Kennaway, J.R., Bangham, J.A., and Coen, E. (2017). Formation and shaping of the *Antirrhinum* flower through modulation of the *CUP* boundary gene. Curr. Biol. *27*, 2610–2622.e3.
8. Kuchen, E.E., Fox, S., de Reuille, P.B., Kennaway, R., Bensmihen, S., Avondo, J., Calder, G.M., Southam, P., Robinson, S., Bangham, A., and Coen, E. (2012). Generation of leaf shape through early patterns of growth and tissue polarity. Science *335*, 1092–1096.
9. Kierzkowski, D., Runions, A., Vuolo, F., Strauss, S., Lymbouridou, R., Routier-Kierzkowska, A.L., Wilson-Sánchez, D., Jenke, H., Galinha, C., Mosca, G., et al. (2019). A growth-based framework for leaf shape development and diversity. Cell *177*, 1405–1418.e17.
10. Lockhart, J.A. (1965). An analysis of irreversible plant cell elongation. J. Theor. Biol. *8*, 264–275.
11. Boudon, F., Chopard, J., Ali, O., Gilles, B., Hamant, O., Boudaoud, A., Traas, J., and Godin, C. (2015). A computational framework for 3D mechanical modeling of plant morphogenesis with cellular resolution. PLoS Comput. Biol. *11*, e1003950.
12. Bozorg, B., Krupinski, P., and Jönsson, H. (2014). Stress and strain provide positional and directional cues in development. PLoS Comput. Biol. *10*, e1003410.
13. Ali, O., Mirabet, V., Godin, C., and Traas, J. (2014). Physical models of plant development. Annu. Rev. Cell Dev. Biol. *30*, 59–78.
14. Sampathkumar, A., Yan, A., Krupinski, P., and Meyerowitz, E.M. (2014). Physical forces regulate plant development and morphogenesis. Curr. Biol. *24*, R475–R483.
15. Smyth, D.R., Bowman, J.L., and Meyerowitz, E.M. (1990). Early flower development in *Arabidopsis*. Plant Cell *2*, 755–767.
16. Poethig, R.S., and Sussex, I.M. (1985). The developmental morphology and growth dynamics of the tobacco leaf. Planta *165*, 158–169.
17. Boudaoud, A., Burian, A., Borowska-Wykręt, D., Uyttewaal, M., Wrzalik, R., Kwiatkowska, D., and Hamant, O. (2014). FibrilTool, an ImageJ plug-in to quantify fibrillar structures in raw microscopy images. Nat. Protoc. *9*, 457–463.
18. Paredez, A.R., Somerville, C.R., and Ehrhardt, D.W. (2006). Visualization of cellulose synthase demonstrates functional association with microtubules. Science *312*, 1491–1495.
19. Hervieux, N., Dumond, M., Sapala, A., Routier-Kierzkowska, A.L., Kierzkowski, D., Roeder, A.H., Smith, R.S., Boudaoud, A., and Hamant, O. (2016). A mechanical feedback restricts sepal growth and shape in *Arabidopsis*. Curr. Biol. *26*, 1019–1028.
20. Peters, W.S., and Tomos, A.D. (1996). The history of tissue tension. Ann. Bot. *77*, 657–665.
21. Hamant, O., Inoue, D., Bouchez, D., Dumais, J., and Mjolsness, E. (2019). Are microtubules tension sensors? Nat. Commun. *10*, 2360.
22. Hamant, O., Heisler, M.G., Jönsson, H., Krupinski, P., Uyttewaal, M., Bokov, P., Corson, F., Sahlin, P., Boudaoud, A., Meyerowitz, E.M., et al. (2008). Developmental patterning by mechanical signals in *Arabidopsis*. Science *322*, 1650–1655.
23. Oliveri, H., Traas, J., Godin, C., and Ali, O. (2019). Regulation of plant cell wall stiffness by mechanical stress: a mesoscale physical model. J. Math. Biol. *78*, 625–653.
24. Kierzkowski, D., Nakayama, N., Routier-Kierzkowska, A.L., Weber, A., Bayer, E., Schorderet, M., Reinhardt, D., Kuhlemeier, C., and Smith, R.S. (2012). Elastic domains regulate growth and organogenesis in the plant shoot apical meristem. Science *335*, 1096–1099.
25. Green, P.B., and King, A. (1966). A mechanism for the origin of specifically oriented textures in development with special reference to *Nitella* wall texture. Aust. J. Biol. Sci. *19*, 421–438.
26. Hejnowicz, Z., Rusin, A., and Rusin, T. (2000). Tensile tissue stress affects the orientation of cortical microtubules in the epidermis of sunflower hypocotyl. J. Plant Growth Regul. *19*, 31–44.
27. Robinson, S., and Kuhlemeier, C. (2018). Global compression reorients cortical microtubules in *Arabidopsis* hypocotyl epidermis and promotes growth. Curr. Biol. *28*, 1794–1802.e2.
28. Cox, H.L. (1952). The elasticity and strength of paper and other fibrous materials. Br. J. Appl. Phys. *3*, 72–79.
29. Bouquin, T., Mattsson, O., Naested, H., Foster, R., and Mundy, J. (2003). The *Arabidopsis lue1* mutant defines a katanin p60 ortholog involved in hormonal control of microtubule orientation during cell growth. J. Cell Sci. *116*, 791–801.
30. Uyttewaal, M., Burian, A., Alim, K., Landrein, B., Borowska-Wykręt, D., Dedieu, A., Peaucelle, A., Ludynia, M., Traas, J., Boudaoud, A., et al. (2012). Mechanical stress acts via katanin to amplify differences in growth rate between adjacent cells in *Arabidopsis*. Cell *149*, 439–451.
31. Wang, G., Wang, C., Liu, W., Ma, Y., Dong, L., Tian, J., Yu, Y., and Kong, Z. (2018). Augmin antagonizes katanin at microtubule crossovers to control the dynamic organization of plant cortical arrays. Curr. Biol. *28*, 1311–1317.e3.
32. Wasteneys, G.O. (2002). Microtubule organization in the green kingdom: chaos or self-order? J. Cell Sci. *115*, 1345–1354.
33. Ehrhardt, D.W., and Shaw, S.L. (2006). Microtubule dynamics and organization in the plant cortical array. Annu. Rev. Plant Biol. *57*, 859–875.
34. Louveaux, M., Julien, J.D., Mirabet, V., Boudaoud, A., and Hamant, O. (2016). Cell division plane orientation based on tensile stress in *Arabidopsis thaliana*. Proc. Natl. Acad. Sci. USA *113*, E4294–E4303.
35. Guan, C., Wu, B., Yu, T., Wang, Q., Krogan, N.T., Liu, X., and Jiao, Y. (2017). Spatial auxin signaling controls leaf flattening in *Arabidopsis*. Curr. Biol. *27*, 2940–2950.e4.
36. Yu, T., Guan, C., Wang, J., Sajjad, M., Ma, L., and Jiao, Y. (2017). Dynamic patterns of gene expression during leaf initiation. J. Genet. Genomics *44*, 599–601.
37. Caggiano, M.P., Yu, X., Bhatia, N., Larsson, A., Ram, H., Ohno, C.K., Sappl, P., Meyerowitz, E.M., Jönsson, H., and Heisler, M.G. (2017). Cell type boundaries organize plant development. eLife *6*, e27421.
38. Haas, K.T., Wightman, R., Meyerowitz, E.M., and Peaucelle, A. (2020). Pectin homogalacturonan nanofilament expansion drives morphogenesis in plant epidermal cells. Science *367*, 1003–1007.
39. Sugimoto, K., Williamson, R.E., and Wasteneys, G.O. (2000). New techniques enable comparative analysis of microtubule orientation, wall texture, and growth rate in intact roots of *Arabidopsis*. Plant Physiol. *124*, 1493–1506.
40. Yamaguchi, T., Yano, S., and Tsukaya, H. (2010). Genetic framework for flattened leaf blade formation in unifacial leaves of *Juncus prismatocarpus*. Plant Cell *22*, 2141–2155.
41. Qi, J., Wu, B., Feng, S., Lü, S., Guan, C., Zhang, X., Qiu, D., Hu, Y., Zhou, Y., Li, C., et al. (2017). Mechanical regulation of organ asymmetry in leaves. Nat. Plants *3*, 724–733.
42. Sassi, M., Ali, O., Boudon, F., Cloarec, G., Abad, U., Cellier, C., Chen, X., Gilles, B., Milani, P., Friml, J., et al. (2014). An auxin-mediated shift toward growth isotropy promotes organ formation at the shoot meristem in *Arabidopsis*. Curr. Biol. *24*, 2335–2342.
43. Skopelitis, D.S., Benkovics, A.H., Husbands, A.Y., and Timmermans, M.C.P. (2017). Boundary formation through a direct threshold-based readout of mobile small RNA gradients. Dev. Cell *43*, 265–273.e6.
44. Ursache, R., Andersen, T.G., Marhavý, P., and Geldner, N. (2018). A protocol for combining fluorescent proteins with histological stains for diverse cell wall components. Plant J. *93*, 399–412.
45. Serrano-Mislata, A., Schiessl, K., and Sablowski, R. (2015). Active control of cell size generates spatial detail during plant organogenesis. Curr. Biol. *25*, 2991–2996.
46. Barbier de Reuille, P., Routier-Kierzkowska, A.L., Kierzkowski, D., Bassel, G.W., Schüpbach, T., Tauriello, G., Bajpai, N., Strauss, S., Weber, A., Kiss, A., et al. (2015). MorphoGraphX: A platform for quantifying morphogenesis in 4D. eLife *4*, 05864.

CellPress
OPEN ACCESS

47. Reinhardt, D., Frenz, M., Mandel, T., and Kuhlemeier, C. (2005). Microsurgical and laser ablation analysis of leaf positioning and dorsoventral patterning in tomato. Development *132*, 15–26.

48. Heidstra, R., Welch, D., and Scheres, B. (2004). Mosaic analyses using marked activation and deletion clones dissect *Arabidopsis* SCARECROW action in asymmetric cell division. Genes Dev. *18*, 1964–1969.

49. Rodriguez, E.K., Hoger, A., and McCulloch, A.D. (1994). Stress-dependent finite growth in soft elastic tissues. J. Biomech. *27*, 455–467.

50. Goriely, A. (2017). The Mathematics and Mechanics of Biological Growth (Springer New York).

51. Besson, S., and Dumais, J. (2011). Universal rule for the symmetric division of plant cells. Proc. Natl. Acad. Sci. USA *108*, 6294–6299.

52. Errera, L. (1888). Uber Zellformen und Seifenblasen. Bot Centralblatt *34*, 395–398.

53. Hofmeister, W. (1863). Zusätze und Berichtigungen zu den 1851 veröffentlichten Untersuchungen der Entwickelung höherer Kryptogamen. Jahrb Wiss Bot *3*, 259–293.

STAR★METHODS

KEY RESOURCES TABLE

REAGENT or RESOURCE	SOURCE	IDENTIFIER
Antibodies		
Mouse anti-α-tubulin	Sigma-Aldrich	Cat# T5168, clone B-5-1-2; RRID: AB_477579
Alexa Fluor 488 conjugated donkey anti-mouse IgG	Invitrogen	Cat# A-21202; RRID:AB_141607
Chemicals, Peptides, and Recombinant Proteins		
FM4-64	Thermo Fisher	Cat# T3166
Propidium iodide (PI)	Sigma-Aldrich	Cat# P4170
Fluorescent Brightener 28 (FB28)	Sigma-Aldrich	Cat# F3543
Agarose, low melting point	Promega	Cat# V2111
Hemicellulase	Solarbio	Cat# H8110-15KU
Macerozyme R-10	Yakult	Cat# L0021
Oryzalin	Dr. Ehrenstorfer	Cat# C15750000
Direct Red 23	Sigma-Aldrich	Cat# 212490
Alpha-amylase	Sigma-Aldrich	Cat# A4551
Gum arabic	Sigma-Aldrich	Cat# G9752
ProLong Gold antifade reagent	Thermo Fisher	Cat# P36930
Low viscosity Spurr Formula Kit	SPI Supplies	Cat# 02680-AB
Experimental Models: Organisms/Strains		
Arabidopsis: *p35S:GFP-MBD*	[22]	N/A
Arabidopsis: *p35S:GFP-Lti6b*	[17]	N/A
Arabidopsis: *3 × YFP-CSI1/POM2* in *mCherry-TUA5*	[41]	N/A
Arabidopsis: Cre-loxP line	[42]	N/A
Arabidopsis: *pWOX1:NLS-GFP*$_3$	[43]	N/A
Arabidopsis: *pPRS:NLS-GFP*$_3$	[43]	N/A
Arabidopsis: *bot1-7*	[30]	N/A
Arabidopsis: *lue1*	[29]	N/A
Arabidopsis: *wox1-101 prs-2*	[4]	N/A
Arabidopsis: *wox1-101 prs-2 as2-1*	[4]	N/A
Software and Algorithms		
Sofa	Open source software	http://www.sofa-framework.org
CellComplex	Python library	http://gitlab.inria.fr/mosaic/cellcomplex
TissueLab	Open source software	http://github.com/VirtualPlants/tissuelab
Blender	Open source software	http://www.blender.org
DRACO-STEM tool	Open source software	http://gitlab.inria.fr/mosaic/draco_stem
Tissue2D	This paper	https://gitlab.inria.fr/mosaic/publications/tissue2d.git

RESOURCE AVAILABILITY

Lead Contact

Further information and requests for resources and reagents should be directed to and will be fulfilled by the Lead Contact, Yuling Jiao (yljiao@genetics.ac.cn).

Materials Availability

This study did not generate new unique reagents.

CellPress
OPEN ACCESS

Data and Code Availability

The published article includes all datasets generated or analyzed during this study.

EXPERIMENTAL MODEL AND SUBJECT DETAILS

Growth conditions

Arabidopsis thaliana plants were grown on soil under long-day (16 h light, LED 150 $\mu Em^{-2}s^{-1}$; 20-22°C day temperature; 60% humidity) or short-day (8 h light) conditions. Others were obtained via crossing and further confirmed by genotyping. For live imaging, inflorescences were dissected and cultured *in vitro* on apex culture medium (ACM) for 5 h until the acquisition [19]. To live image the leaf growth, vegetative meristems (cultured on soil under short-day for 30 days) were dissected carefully and then cultured *in vitro* on ACM for 5 h prior to the acquisition. For agarose gel sectioning, plants were grown in 1/2 MS medium at 22°C under short day conditions (8 h light/16 h dark) for 15 days. For semi-thin sectioning, *Arabidopsis* plants were grown in 1/2 MS medium at 22°C under long day conditions (16 h light/8 h dark) for 15 days.

Tomato (*Solanum lycopersicum*) cultivar M82 was grown in 1/2 MS medium at 25°C under long day conditions (16 h light/8 h dark) for one week until the fifth to seventh plastochron stage as previously described [41]. Shoot apices were dissected and grown in the tissue culture medium (MS medium supplemented with 1 μg/mL *t*-zeatin) for additional 2 to 3 days.

METHOD DETAILS

Visualization of microtubules

Live imaging of microtubule was carried out according to [17, 22]. To obtain cortical microtubule signals in young leaf primordia, one cotyledon was removed from young seedling (*p35S:GFP-MBD*) at 4 DAS (days after stratification) in order to expose the leaf primordia. Imaging 3 × YFP-CSI1/POM2 in mCherry-TUA5 background on stage 4-5 floral primordia was performed on a spinning disk microscope fitted with a CMOS camera using a 100 × oil-immersion objective (Plan Apo TIRF, NA 1.45). We recorded several multi-dimensional time series with typical exposure times of 300 ms for both 3 × YFP-CSI1/POM2 and mCherry-TUA5, intervals of 60 s for total duration of up to 15 min, and *z*-steps of 300 nm. YFP was excited using 491 nm and mCherry with 561nm lasers. For immunostaining of microtubule, old leaf primordia were removed and the shoot apices were collected into the freshly prepared fixative (4% paraformaldehyde, 0.5% glutaraldehyde, 0.3% Tween-20, 0.3% Triton X-100) in MTSB (50 mM PIPES, 5 mM $MgSO_4 \cdot 7H_2O$, 5 mM EGTA, pH = 7.0). Tissues were vacuum infiltrated at −0.075 MPa (550 mm Hg) for 10 min three times, followed by an additional 3 h fixation at room temperature. After three times of washing by MTSB (20 min per wash), tissues were embedded into 6% Low Melting Agarose. 40-50 μm transverse sections were obtained using a Leica VT1000S vibratome and collected into MTSB solution in a circle marked by PAP pen (Daido Sangyo Co., Cat# 1-5902-01) on a poly-lysine treated slide. The subsequent steps were all performed by exchanging different solutions in this PAP pen circle on the slide. For *Arabidopsis* samples, sections were digested with 1% hemicellulase, 0.1% Macerozyme R-10 and 1% Triton X-100 in MTSB for 15 min at room temperature, followed by incubation in 1% Triton X-100 in MTSB for 15 min, and then washed three times with 1 × TBS (20 mM Tris-HCl, 150 mM NaCl, pH = 8.0) for 5 min each time. For tomato samples, sections were digested with 1% hemicellulase and 1% Triton X-100 in MTSB for 15 min at room temperature, followed by three times wash with 1 × TBS for 5 min each time. Sections were incubated in mouse anti-α-tubulin antibody at 1:800 dilutions with 1% BSA in 1 × TBS overnight at 4°C in a humid box. Sections were washed three times with 1 × TBS for 10 min each time, and incubated in Alexa Fluor 488 conjugated donkey anti-mouse IgG at 1:500 dilutions with 1% BSA in 1 × TBS at 37°C in a humid box for 2 h in darkness. After washing three times with 1 × TBS for 10 min each time, sections were stained with 1 μg/mL DAPI for 15 min in darkness to visualize nuclei. Sections were washed in 1 × TBS for 10 min and mounted in ProLong Gold antifade reagent before imaging.

Oryzalin treatment

6.4 mM stock solution of oryzalin (dissolved in DMSO) was mixed with pre-warmed lanolin in a ratio of 1:9, and gave rise to a final concentration of 640 μM oryzalin which was effective to trigger microtubule depolymerization while kept the organ continue growing [42]. Equal amount of DMSO was employed as the untreated control. The paste of chemicals was performed on P_2 of dissected tomato shoot apices by syringe tips. For treatment on flower organs, dissected inflorescences were immersed in the water containing 20 μg/mL oryzalin for three h at room temperature and then washed in water twice [22], the same treatment was carried out every day. Equal amounts of DMSO were used as control. Images were obtained 48 h after the treatment.

Agarose gel sectioning

Agarose gel sectioning and staining procedure was performed essentially as previously described [43, 44] with minor modifications. Older leaf primordia and cotyledons were removed from *Arabidopsis* and tomato shoot apices using a syringe needle under a dissecting microscope. The shoot apices were collected into the freshly prepared fixative solution containing 4% paraformaldehyde and 0.015% Tween-20 in 1 × PBS (pH = 7.0). Vacuum infiltration at −0.075 MPa (550 mm Hg) was performed on *Arabidopsis* tissues for twice with 10 min each time, and on tomato tissues for three times with 10 min each time. Tissues were washed three times (10 min per time) in 1 × PBS and embedded into 6% Low Melting Agarose. 40-50 μm transverse sections were obtained using a Leica VT1000S vibratome.

For examining the cell division pattern or reporter gene expression domains, the sections were stained by 0.01% Fluorescent Brightener 28 (FB28) in 1 × PBS for 20 min in darkness to label the cell walls, and then washed three times (5 min per time) in 1 × PBS. For observing the cellulose microfibril orientation, the sections were stained by 0.01% Direct Red 23 (also known as Pontamine Fast Scarlet 4B) in 1 × PBS for 20 min in darkness to label the cellulose microfibrils, and then washed three times (5 min per time) in 1 × PBS. Sections were mounted in 90% glycerol in 1 × PBS, and were imaged using a Nikon A1 confocal laser scanning microscope.

Modified pseudo-Schiff-PI (mPS-PI) staining

mPS-PI staining was performed as previously reported [45] with minor modifications. Tomato shoot apices were dissected from the plants and dehydrated through 15%, 30%, 50%, 70%, 85%, 95% and 100% ethanol for 15 min each concentration at room temperature. The tissues were incubated in 100% ethanol overnight at room temperature. Dissect tissues in 100% ethanol on a 3% agar plate by removing older leaf primordia. Shoot apices containing P_2 or P_3 were finally dissected and transferred into a 96 well plate, followed by a rehydration through 95%, 85%, 70%, 50%, 30%, 15% ethanol and sterile water for 15 min each at room temperature with gentle shaking. Tissues were incubated in alpha-amylase mixture (0.03% alpha-amylase dissolved in 20 mM pH = 7.0 phosphate buffer, 2 mM NaCl and 0.25 mM $CaCl_2$) overnight at 37°C. After rinsing in sterile water, tissues were incubated in 1% periodic acid in water for 30 min at room temperature. After rinsing in sterile water, tissues were stained in freshly made Schiff reagent (20 μg/mL propydium iodide in 2% sodium bisulphite and 1.25% HCl solution) for 2 h in the darkness at room temperature. The tissues were rinsed with sterile water and transferred onto groove slides. The tissues were cleared in chloral hydrate solution (mixture of 8 g chloral hydrate, 1 mL glycerol and 2 mL sterile water) and mounted in Hoyer's medium (mixture of 40 g chloral hydrate, 6 g gum arabic, 5 mL glycerol and 10 mL sterile water) for at least 2 days at room temperature.

Because of the large size of tomato shoot apices, tapes were often adhered onto the slides to lift up the coverslip and leave enough space between the slides and coverslip so that the shoot apices can move. Before the confocal microscopy, one can adjust the tissues to the desired orientation by carefully moving the coverslip under a stereomicroscope.

Confocal microscopy

Zeiss LSM 700 laser-scanning confocal microscope equipped with water immersion objectives (W Plan-Apochromat 40×/1.0 DIC and W Plan-Apochromat 63×/1.0 M27) and Nikon A1 confocal laser scanning microscope (Nikon Plan Apo VC 20×/0.75 DIC, Nikon Plan Apo VC 60×/1.40 oil and Nikon Plan Apo VC 100×/1.40 oil) were used for fluorophores detection. To detect DAPI and FB28 staining, a 405 nm laser line was used for excitation and emission was collected at 425–475 nm. To detect Green Fluorescent Protein (GFP) and Alexa Fluor 488 signal, a 488 nm laser line was used for excitation and emission was collected at 500–530 nm. To detect PI and Direct Red 23 staining, a 561 nm laser line was used for excitation and emission was collected at 660–740 nm.

Image processing and analysis

To visualize the 3D structure of organs, Zeiss ZEN2 software was used to make a 3D transparent projection of the signal. Flowers harboring *p35S:GFP-Lti6b* marker or stained with propidium iodide (100 μM for five minutes) were examined with Zeiss LSM 700 laser-scanning confocal microscope. The width and thickness of leaf and sepal cross sections were measured by using Fiji software (https://fiji.sc). The aspect ratios (width/thickness) were calculated by using Microsoft Excel software. For the analysis of cortical microtubule at the surface, the microtubule signals were projected by using Zeiss ZEN2 software and processed as described previously [22]. For the analysis of cortical microtubules in the ad-abaxial direction, the 'Reslice' function of Fiji software was used to extract CMT signals followed by a maxima z-projection of newly generated stacks to obtain the microtubule orientation along the ad-abaxial walls. Fibril tool was used to quantify microtubule anisotropy on all membranes. For cell division orientation measurement, the z stack optical cross-sections of *Arabidopsis* (by FB28 staining) leaf primordia and tomato (by mPS-PI staining) were analyzed by NIS-Elements AR Analysis software affiliated to Nikon A1 confocal laser scanning microscope. For inner cells, the angle between the new cell wall and medio-lateral axis were measured. For epidermal cells, the angle between the new cell wall and the tangent of the corresponding cell were measured. The curvature maps of young flowers were obtained by MorphoGraphX software [46]. Gaussian curvature was calculated with a neighboring of 10 μm.

Microsurgery and scanning electron microscopy

Microsurgery was performed by making an incision between the SAM and incipient primordium (I_1) using a syringe needle (0.3 mm, BD Ultra-Fine Insulin Syringe) under a dissecting microscope as previously described [47]. The incised shoot apices were allowed to grow for four days, followed by transverse agarose gel sectioning of radialized leaf primordial generated from the incised I_1.

Tissue fixation for scanning electron microscopy was carried out using a quick method as previously described. Briefly, shoot apices were fixed in pure methanol for 15 min and then dehydrated in 100% ethanol for 30 min at room temperature. After one change of 100% ethanol, the tissues were stored in 100% ethanol overnight at room temperature. Tissues were dried with CO_2 in a critical point drier and coated with gold in a sputter coater. Tissues were imaged using a Hitachi S-3000N variable pressure scanning electron microscope at an accelerating voltage of 5 kV. For scanning flower organs, fresh plant materials were observed with HIROX SH-3000 tabletop microscope equipped with a cool stage. The temperature was set at −20°C and accelerating voltage was 5 kV.

CellPress
OPEN ACCESS

Cre-loxP based cell lineage tracing analysis

A previously reported Cre-loxP based recombination system was used to identify cell division orientations in *Arabidopsis* leaf primordia, in which clonal cell files were marked by ER-localized GFP after a short period of heat shock [48]. 15-day-old *Arabidopsis* seedlings grown on 1/2 MS plates under the short day condition were used for cell lineage tracing analysis. Seedlings were heat shocked for 40 min at 37°C in the plates with closed lids. After the heat shock, the seedlings were put back to the short day condition and continued to grow for 24 h, 48 h and 72 h. Then the agarose gel sectioning and FB28 staining were performed on P_4/P_5 leaf primordia of heat shocked seedlings to detect the GFP expression with a Nikon A1 confocal laser scanning microscope.

No detectable GFP expression was found 24 h or 48 h after the heat shock, while a few cells showed GFP expression 72 h after the heat shock. The seedlings without a heat shock but still continued to grow for 72 h were set as the negative controls, in which no GFP expression was observed in leaf primordia.

Semi-thin sectioning

The oldest true leaves of *Arabidopsis* 15-day-old plants growing in the long day condition were fixed in FAA solution under vacuum for 3 × 10 min at −0.07 MPa, and stayed overnight at 4°C. After a dehydration in an ethanol series to 100% ethanol, tissues were embedded into the SPI low viscosity Spurr Formula Kit. 2 μm-thick sections were obtained using a Leica RM 2265 rotary microtome and stained with 1% toluidine blue in water supplemented with 1% sodium tetraborate at 65°C for 20-30 min. Sections were mounted in 50% glycerol for optical microscopy.

Cell wall thickness measurement

Tomato and *Arabidopsis* shoot apices were fixed with 5% glutaraldehyde in 1 × PBS under vacuum for 4 × 10 min at −0.07 MPa, and stayed overnight at 4°C. Tissues were washed in 1 × PBS for 4 × 15 min at room temperature and further fixed in 1% OsO_4 for 4 h at room temperature. After the rinse by 1 × PBS for 4 × 15 min, tissues were dehydrated in an ethanol series to 100% ethanol before being embedded into the SPI low viscosity Spurr Formula Kit. 70 nm-thick cross-sections of tomato P_3 and *Arabidopsis* P_4 were obtained using a Leica EM UC6 rotary microtome and imaged using a Hitachi HT7700 electron microscope. Images were quantified for cell wall thickness by ImageJ software.

Model description

General description

We model tissues as multicellular alveolate structures, each cell being described as a set of connected walls, loaded with a steady and uniform pressure. Both our 2D and 3D models account for reversible (i.e., elastic) and irreversible (i.e., growth) deformations.

We work in the framework of morphoelasticity [49, 50], in which total deformation is classically modeled as the product of a growth deformation and an elastic deformation. In the 3D model, this is implemented following [23], through a multiplicative decomposition of the total 2D deformation gradient **F** into an elastic (**A**) and a growth (**G**) component (see Methods S1 for details):

$$\mathbf{F} = \mathbf{A} \cdot \mathbf{G}. \tag{1}$$

Similarly, in the 2D approach, the total elongation of the edges is expressed multiplicatively via a reversible and an irreversible term (see Methods S2 for details):

$$l = (1 + \varepsilon) l_0 \tag{2}$$

where l, ε and l_0 respectively account for the total length, the elastic strain (i.e., the wall relative elongation) and the resting length of walls.

We postulate that, constitutively, the strain energy of the material is a function of the elastic part of the deformation only. Accordingly, the strain energy function used in the 3D (resp. 2D) model is a function of **A** (resp. ε) only.

In both models, we assume that growth occurs much slower than elastic relaxation. This allows us to treat the growth and elastic regimes separately. Each step of the algorithms (implemented for both models) can be decomposed in sub-operations (detailed next) consisting of (*i*) computing the mechanical equilibrium, which provides **A** (resp. ε); (*ii*) computing growth by incrementally modifying **G** (resp. l_0). In both models, an additional optional step corresponding to the implementation of the mechanical feedback and the associated modification of the mechanical wall properties can be carried out. Finally, the 2D model can also perform a cell division step.

Details about their numerical implementations, as well as parameter estimates are given in Methods S1 (for the 3D model) and S2 (for the 2D model).

Mechanical models

In the 3D model, we model the cell walls as a set of triangular finite elements labeled by (τ) under plane stress. Following [11], we modeled elasticity via the anisotropic Saint Venant-Kirchhoff energy function, which in our FE framework translates into the following total energy:

$$\mathscr{E}_{\mathrm{E}} = \sum_{\tau \in T} \varepsilon^{(\tau)} S^{(\tau)} \times \frac{1}{2} \mathbf{E}^{(\tau)} : \mathbb{C}^{(\tau)} : \mathbf{E}^{(\tau)} \tag{3}$$

where $\mathbb{C}^{(\tau)}$, $\mathbf{E}^{(\tau)}$, $S^{(\tau)}$ and $\varepsilon^{(\tau)}$ depict respectively the fourth order elasticity tensor, the Green-Lagrangian strain, the surface area and thickness of triangle$_\tau$. See Methods S1 for details.

Similarly, in the 2D model, walls are modeled by 1D linear springs (indexed by *(e)* hereafter) associated with the elastic potential energy potential:

$$\mathscr{E}_E = \sum_e \frac{k^{(e)}}{2}\left(l^{(e)} - l_0^{(e)}\right)^2 \quad (4)$$

where the sums over indices e is carried out over the walls of the considered tissue. The variable $l^{(e)}$ corresponds to the length of wall *e*. Parameters $k^{(e)}$ and $l_0^{(e)}$ stand for the spring constant and the resting length of wall *(e)*. See Methods S2 for details.

Growth models

To model growth of the walls in our 3D framework we use the growth model developed in [11]. This model describes an exponential growth based on strain described in term of *rate of growth* as:

$$\dot{\mathbf{G}} \cdot \mathbf{G}^{-1} = \Phi\langle \mathbf{E} - E_{\text{thr}}\,\mathbf{I}\rangle. \quad (5)$$

The previous expression provides a multidimensional extension of Lockhart's 1D model [10]. Parameters Φ and E_{thr} respectively depict the wall extensibility and yield threshold; $\langle\cdot\rangle$ depicts the tensor ramp function.

The growth equation used in the 2D model reads:

$$\frac{1}{l_0^{(e)}}\frac{dl_o^{(e)}}{dt} = \gamma_g h_{ng}\left(\varepsilon_j^{(e)}, \varepsilon_{\text{th}}\right) \quad (6)$$

where $\varepsilon^{(e)}$ corresponds to the elastic strain of the edges at equilibrium. The threshold behavior of the growth law is assured by the Hill function h_{ng}, see Methods S2 for details. The parameters γ_g and ε_{th}, in the right-hand side of Equation 6, are equivalent to Φ and E_{thr} in Equation 5.

Note a slight difference here between the 2D and 3D models: The Hill function in the 2D model gives a saturating property to the growth law, such property being absent of the 3D model using an unbounded ramp function. This didn't change the dynamics in simulations with feedbacks and cell division but prevented control simulations (without feedback and division) to grow unrealistically fast.

Stress feedback

To model the directional stress feedback in the 3D model, we use the approach detailed in [23]. This model details the dependency of CMT organization upon stress, and the CMT-guided cellulose deposition. The dynamics of cellulose deposition within the walls is expressed through an ordinary differential equation (ODE) describing the microtubule-guided synthesis of cellulose fibers:

$$\dot{\rho}(\theta) = k_{\text{on}}\phi(\theta) - k_{\text{off}}\rho(\theta) \quad (7)$$

where $\rho(\theta)$ and $\phi(\theta)$ respectively depict the local angular density of cellulose fibers and of CMTs in the direction θ. The coefficients k_{on} and k_{off} are kinetic constants associated with cellulose polymerization/depolymerization. The cell wall elasticity tensor $\mathbb{C}$ is a function of the cellulose angular distribution ρ; see Methods S1 for details.

In the 2D model, the elastic properties of the walls are encoded within the spring constants $k^{(e)}$ associated to the edges. By definition, spring constants are functions of the resting length of the corresponding edges: $k(e) = \tilde{k}^{(e)}/l_0^{(e)}$, where $\tilde{k}^{(e)}$ is an *effective spring constant* that only depends on the material properties of the walls and their cross section (that we assumed constant). Since the stress feedback would only modify the material properties of the considered walls, we expressed the effective spring constant of the edges as a Hill function of the edge tension, see Methods S2 for details:

$$\tilde{k}^{(e)} = \tilde{k}_0^{(e)}\left(1 + \gamma_s h_{ns}\left(f^{(e)}, f_{th}\right)\right). \quad (8)$$

Similarly to γ_g and ε_{th} in Equation 6, γ_s and f_{th} in Equation 8 respectively correspond to the amplitude and the inflection point of the Hill function. The variable $f^{(e)}$ is the tension in edge *(e)* at mechanical equilibrium and $k_0^{(e)}$ is the initial spring constant. Note that Equation 8 corresponds to the steady state of an ODE similar to Equation 7; see Methods S2 for details.

Cell division (in 2D model only)

We assumed that cell division was triggered once cells had reached a threshold size. In order to obtain two daughter cells of similar sizes, we constrained the newly added edge to pass through the mother cell centroid. We fixed the orientation of epithelial cell divisions normal to the exterior surface of the tissue. For inner tissues, the definition of the division plane orientation being still an open question, we tested three possible mechanisms:

- A geometrical rule: cells divide along the shortest axis [51, 52].
- A mechanical rule: cells divide along the largest stress direction [22].
- A growth-based rule: cells divide perpendicular to their axis of maximal expansion [53].

QUANTIFICATION AND STATISTICAL ANALYSIS

For quantification of aspect ratios in *Arabidopsis* sepals (as shown in Figures 2, 5, and 7), we measured the straight distance between sepal margins as the width, and the largest distance between the adaxial and abaxial surface as the thickness. Measurements were

performed on the optical sections of live imaging. Data represents Mean ± SD of samples pooled from at least three biological replicates, and n indicates the number of sepals used for quantification.

For quantification of aspect ratios in *Arabidopsis* and tomato leaves (as shown in Figure 6 and Figure S1), the width is defined as twice the medio-lateral axis connecting the center to the farthermost points on the outline of a leaf cross-section, and the thickness is defined as the distance between the adaxial and abaxial surface in the half blade. Measurements were performed on the optical sections of PI staining leaf primordia (data shown in Figure 6). For the measurements shown in Figures S1, optical sections of mPS-PI treated tomato leaf primordia from P_2 to P_4, agarose gel sections of FB28 stained *Arabidopsis* leaf primordia from P_2 to P_7, and semi-thin sections of Spurr-embedded *Arabidopsis* mature leaves, data were collected from at least three biological replicates and one representative sample for each section at each stage was shown.

For CMT alignment analysis (as shown in Figures 1 and 5), degrees of CMT anisotropy were measured in several *Arabidopsis* sepals. Data represents Mean ± SD of samples pooled from at least three biological replicates, and n indicates the number of sepals used for quantification.

For the cell division pattern assay (as shown in Figures 2 and S6), division orientation of both inner cells and epidermal cells were measured in several individual leaf primordia of *Arabidopsis* and tomato from different biological replicates. The distribution of cell division angles in one representative leaf primordium sample was shown for each treatment; n indicates the number of cells where division planes were measured.